

## RESEARCH ARTICLE

# A method to derive satellite PAR albedo time series over first-year sea ice in the Arctic Ocean

Julien Laliberté<sup>1\*</sup>, Eric Rehm<sup>1</sup>, Borge Hamre<sup>2</sup>, Clémence Goyens<sup>3</sup>, Donald K. Perovich<sup>4</sup>, and Marcel Babin<sup>1</sup>

Deriving sea ice albedo from spaceborne platforms is of interest to model the propagation of the photosynthetically available radiation (PAR) through Arctic sea ice. We show here that use of the Moderate Resolution Imaging Spectroradiometer (MODIS) operational surface reflectance satellite product to derive albedo in the PAR spectral range is possible. To retrieve PAR albedo from the remote sensing surface reflectance, we trained a predictive model based on a principal component analysis with in situ and simulated data. The predictive model can be applied to first-year sea ice surfaces such as dry snow, melting snow, bare ice and melt ponds. Based on in situ measurements and the prescribed atmospheric correction uncertainty, the estimated PAR albedo had a mean absolute error of 0.057, a root mean square error of 0.074 and an  $R^2$  value of 0.91. As a demonstration, we retrieved PAR albedo on a 9-km<sup>2</sup> area over late spring and early summer 2015 and 2016 at a coastal location in Baffin Bay, Canada. On-site measurements of PAR albedo, melt pond fraction and types of precipitation were used to examine the estimated PAR albedo time series. The results show a dynamic and realistic PAR albedo time series, although clouds remained the major obstacle to the method. This easy-to-implement model may be used for the partitioning of PAR in the Arctic Ocean and ultimately to better understand the dynamics of marine primary producers.

**Keywords:** Sea ice, Photosynthetically available radiation, Surface reflectance, Phytoplankton, Satellite

## 1. Introduction

Contrary to previous assumptions, under-ice phytoplankton blooms can be significant (Lowry et al., 2014), especially in the context of a thinner, more transparent Arctic sea ice cover (e.g., Horvat et al., 2017). To identify an under-ice bloom on a rather local scale, ice camps (Mundy et al., 2014; Oziel et al., 2019), oceanographic cruises (Arrigo et al., 2014; Randelhoff et al., 2019), ice-tethered buoys (Laney et al., 2014; Hill et al., 2018), bio-Argo floats (Mayot et al., 2018; Randelhoff et al., 2020) and sediment traps (Fortier et al., 2002) can be used. To recognize the extent of under-ice blooms at pan-Arctic scale, however, the in situ data from these cumbersome, expensive observational approaches is insufficient. Over synoptic spatial scales, a detailed description of abiotic factors controlling phytoplankton, such as the under-ice photosynthetically available radiation (PAR), could provide a better

understanding of the changing Arctic Ocean ecosystem (Arrigo et al., 2012; Lewis et al., 2019).

From a radiative transfer perspective, without a full description of the above-surface radiance distribution and the inherent optical properties of sea ice, accurately estimating under-ice PAR is difficult. A solution envisioned by several researchers (e.g., Assmy et al., 2017; Horvat et al., 2017; Stroeve et al., 2021) is to estimate the above-surface plane irradiance, reduce it by the energy leaving the sea ice surface (conveyed quantitatively by the albedo) and apply a log-linear decrease of energy with depth, scaled by the thickness of the medium. Surface albedo is defined as the ratio between solar radiation reflected by Earth's surface and solar radiation incident on the surface. Optically, it summarizes the interaction between the surface-incident radiation and everything at and beneath the atmospheric lower boundary. It is a key variable for determining downward irradiance above (Grenfell and Perovich, 2004; Laliberté et al., 2021) and below sea ice in the Arctic Ocean (Ebert et al., 1995; Nicolaus et al., 2010). Therefore, mapping PAR under sea ice and eventually assessing under-ice primary production at a large scale over the Arctic Ocean requires robust estimates of surface albedo based on remote sensing data.

A coarse solution to obtain PAR albedo over large scales is to use empirically fixed PAR albedo values for given surface categories (Castellani et al., 2017; Horvat et al., 2017; Lange et al., 2017). But this approach implies

<sup>1</sup>Département de biologie et Québec-Océan, Takuvik Joint International Laboratory, Laval University (Canada)—CNRS (France), Québec, Québec, Canada

<sup>2</sup>Department of Physics and Technology, University of Bergen, Bergen, Norway

<sup>3</sup>Royal Belgian Institute of Natural Sciences, Brussels, Belgium

<sup>4</sup>Thayer School of Engineering, Dartmouth College, Hanover, NH, USA

\* Corresponding author:  
Email: [julien.laliberte@gmail.com](mailto:julien.laliberte@gmail.com)

determining relative areal proportions of the different surface categories from grid cells much larger than the surface features (Rösel et al., 2012; Wright and Polashenski, 2020), leading to potentially important uncertainties. It also generally assumes too little spectral variation per surface category (Tschudi et al., 2008; Yackel et al., 2018). In parallel, dynamic semi-empirical approaches to derive seasonal patterns in sea ice evolution modulated by the timing of events (Perovich and Polashenski, 2012; Arndt and Nicolaus, 2014; Laliberté et al., 2021) can be used with satellite-retrieved information based on, for instance, polarized backscatter (Perovich et al., 2007) and a library of representative albedo values (e.g., De Abreu et al., 1995) to obtain the seasonal evolution of visible albedo. While suitable over large spatial and temporal scales, the spatial resolution of scatterometers or passive microwave radiometers (generally 25 km) would preclude the use of this approach near land where the signal would be contaminated. We also anticipate that, in many cases, 25 km may be too large to examine the relation between the icescape, phytoplankton drift and the dynamic of under-ice phytoplankton blooms. Finally, a more direct route is to estimate albedo using mature satellite-derived broadband albedo products, specifically available for the Polar Oceans, such as the Extended AVHRR Polar Pathfinder dataset, computed twice daily from AVHRR channels 1 and 2 (Key et al., 2016). These existing operational albedo products derived from remote sensing data have been developed to address heat flux at the Earth surface and related thermodynamic processes. Therefore, they are defined for the full spectrum of solar energy, between 300 and 3000 nm. The spectral range that is relevant to primary production by phytoplankton under sea ice, however, is the range of visible wavelengths (400–700 nm). Typically, when trying to assess visible light available under Arctic (Stroeve et al., 2021) or Antarctic (Pinkerton and Hayward, 2021) sea ice, the method consists of multiplying these broadband shortwave estimates by a conversion factor to reduce the wavelength range to the visible band. A conversion of a broadband albedo to a visible one is possible, but it is highly sensitive to atmospheric conditions and surface physical properties (Grenfell and Perovich, 2008), adding avoidable uncertainties to these estimates.

The use of visible spaceborne sensors should be a good alternative approach. Visible satellite imagery typically has high spatial resolution, sufficient radiometric signal-to-noise ratio, and a large swath to provide overlaps of adjacent orbits towards high latitudes to help overcome the prevalent cloud cover (**Figure 1**). As such, the mature and widely used moderate resolution imaging spectroradiometer (MODIS) land spectral albedo product (Schaaf et al., 2002) is built upon clear-sky atmospherically corrected surface reflectances from the combined Aqua and Terra observations. However, this approach cannot provide an estimate of sea ice albedo in the visible range at a relatively high spatial resolution because of the highly dynamic Arctic surface. Because of sea ice drift, changes in temperature, and precipitation, the extreme seasonal cycle of sea ice albedo over the Arctic Ocean is characterized by short

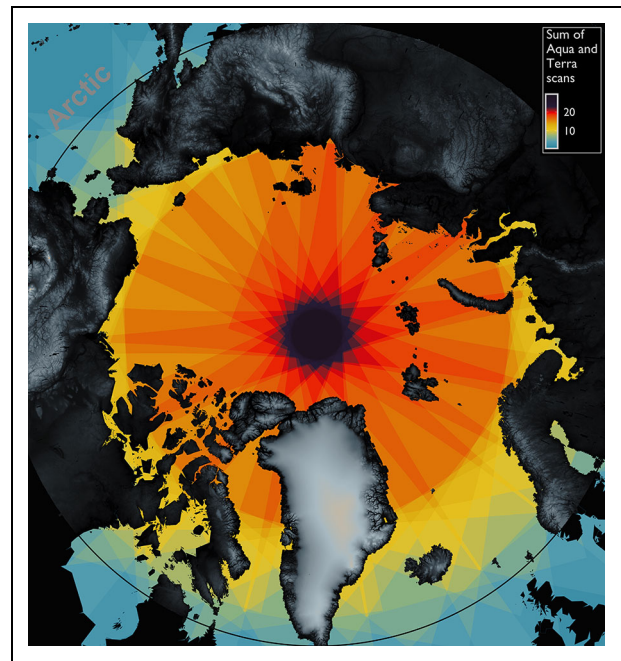


**Figure 1. Number of MODIS daily scans over the Arctic Ocean.** Combining scans from both Aqua and Terra platforms is a powerful way to observe the Arctic Ocean surface. The figure depicts the spatial distribution of the total number of Aqua and Terra scans for which the sun was above the horizon at the center of the orbital track on June 20, 2015. Digital surface model from Porter et al. (2018). DOI: <https://doi.org/10.1525/elementa.2020.00080.f1>

periods of drastic change and is overall more variable than any other planetary surface. The continuous evolution of surface properties precludes the collection of sufficient multiangle observations over each pixel that would constrain a retrieval of albedo via inversion of a multidirectional anisotropy model (Lutch et al., 2000).

In this study, we used the satellite-derived surface reflectance product that is input to the operational MODIS spectral albedo algorithm. However, instead of generating albedo for a wide diversity of planetary surfaces and over a variety of spectral and broad bands, we focused on Arctic sea ice and the spectral range relevant to primary production modelling within the limited sun and viewing geometries of the polar latitudes. First, we present a brief theoretical background to describe the relation between surface reflectance and albedo. Second, we describe the model and the data used to develop it. Third, the model is evaluated with field measurements and is applied to a specific region in the Canadian Arctic. Finally, the model limitations are discussed.

## 2. Method

### 2.1. Theoretical background

We used the surface reflectance as a starting point to derive albedo. It is a directional quantity that is routinely derived by satellites. For any geophysical surface and given illumination, the radiance distribution leaving that surface is expected to emerge with some degree of directional

irregularity (Goyens et al., 2018). Surfaces with such reflectance properties are said to be anisotropic. In contrast, under the same illumination, a surface with isotropic reflectance properties would reflect radiance equally in all directions. For our purpose, we defined the surface reflectance (SREF) as the ratio of sea-ice-leaving radiance  $L_r(\theta_i, \phi_j)$  to sea-ice-incident irradiance  $E_d$  ( $\text{W m}^{-2}$ ) normalized to a perfectly reflecting isotropic surface ( $1/\pi, \text{sr}^{-1}$ ):

$$SREF = \frac{L_r(\theta_i, \phi_j) \pi}{E_d} \quad (1)$$

In Equation 1,  $L_r$  ( $\text{W m}^{-2} \text{sr}^{-1}$ ) is the radiance in the upward direction at given zenith ( $\theta_i$ ) and azimuthal ( $\phi_j$ ) angles (Nicodemus et al., 1977). The subscripts  $i$  and  $j$  refer to a specific narrow direction for which the radiance is assumed homogeneous within a small finite field-of-view. Surface reflectance is a widely used measurable quantity (as opposed to conceptual; see Schaepman-Strub et al., 2006) often named hemispherical-conical reflectance factor (HCRF, dimensionless). Surface reflectance may refer to a particular satellite band, in which case

$$SREF(\theta_i, \phi_j, b, d) = \sum_{\lambda} SREF(\theta_i, \phi_j, \lambda) \cdot RSR(b, d, \lambda) \Delta\lambda \quad (2)$$

with  $RSR(b, d, \lambda)$  as the relative spectral response for band  $b$  and sensor  $d$ . The relative spectral response indicates the quantum efficiency of the sensor at a particular wavelength.

Our goal was to achieve PAR albedo estimates from the satellite-derived surface reflectance. The albedo ( $\alpha$ , dimensionless) is a compilation of the surface reflectances from all directions in a given band or spectral interval. If the albedo is computed for an isotropic surface, a surface reflectance of any direction is equal to its albedo. The albedo is defined as the ratio of upwelling planar irradiance  $E_u$  ( $\text{W m}^{-2}$ ) to downwelling planar irradiance, and is computed as an angular weighted average of the surface reflectances over all discrete quadrilateral regions  $\Delta\theta_i \Delta\phi_j$  of the upper hemisphere:

$$\begin{aligned} \alpha &= \frac{E_u}{E_d} = \frac{\int_{\phi=0}^{2\pi} \int_{\theta=\pi/2}^{\pi} L_r(\theta, \phi) \cos\theta \sin\theta d\theta d\phi}{E_d} \\ &\approx \sum_i \sum_j \left[ \frac{L_r(\theta_i, \phi_j) \cos\theta_i \sin\theta_i}{E_d} \Delta\theta_i \Delta\phi_j \right] \\ &= \sum_i \sum_j \left[ \frac{SREF_{ji} \cos\theta_i \sin\theta_i}{\pi} \Delta\theta_i \Delta\phi_j \right] \end{aligned} \quad (3)$$

Here, radiances are approximated by non-equal regions of assumed constant fluxes spanning the entire upper hemisphere, and their conversion to a planar irradiance requires accounting for their projected area. It follows that the angular weighted sum of all surface reflectances

approximates the albedo. Spectrally, the wavelength-integrated PAR albedo ( $\alpha_{PAR}$ ) is defined as:

$$\alpha_{PAR} = \frac{\int_{\lambda=400}^{700} \alpha(\lambda) E_d(\lambda) d\lambda}{\int_{\lambda=400}^{700} E_d(\lambda) d\lambda} \quad (4)$$

with  $E_d(\lambda)$  as the spectral irradiance incident on the surface. To account for the variability of the reflectance from sea ice surfaces based on solar and viewing geometries (both known for any MODIS pixel), an anisotropy reflectance factor (ARF) can be defined by normalizing the surface reflectance (SREF in Equation 1) with the albedo (Equation 3). This normalization allows us to assess the angular and spectral dependence of contrasted melting surfaces using a common scale. The ARFs take on values below unity, equal to unity and above unity, depending on the viewing angle. Values equal to unity imply that the surface reflectance in that viewing direction is numerically equal to the albedo. An ARF value below (above) unity implies that the surface reflectance that is being recorded in that direction is numerically smaller (greater) than what would be recorded if the surface was isotropic; using the surface reflectance from that direction and simply assuming that the surface is isotropic would lead to an underestimation (overestimation) of the albedo.

### 2.2. Approach

Because reflectance from the sea ice surface is anisotropic, we needed a model to tie MODIS surface reflectance to the albedo. Each available satellite viewing geometry represents a specific observation of surface conditions and sample of anisotropic sea ice surfaces. Depending on the timing and the location, the surface could be composed of melting snow, bare ice and/or melt ponds. For a given reflectance measurement, we have no way of knowing the composition of the surface element mixture that was sampled, so we cannot apply an anisotropy correction based on a surface typology.

We solved this inverse problem using a well-defined and restricted approach. First, rather than deriving albedo for a wide range of planetary surfaces and spectral domains, we focused on a single surface cover class and the visible range. Second, we set a narrow frame of measurement conditions in which the departure from isotropy is small. In fact, our model only needs to represent a subset of surface anisotropy matching the sun and viewing geometry of the Arctic scanned by MODIS, in addition to the small spectral dependence of the surface over the visible range (discussed in this section).

When the MODIS albedo (code MCD43) is produced over land using the operational algorithm of Schaaf et al. (2002; 2011), an albedo retrieval is computed over sixteen days of satellite observation. On global scale, this was deemed the best tradeoff between the number of

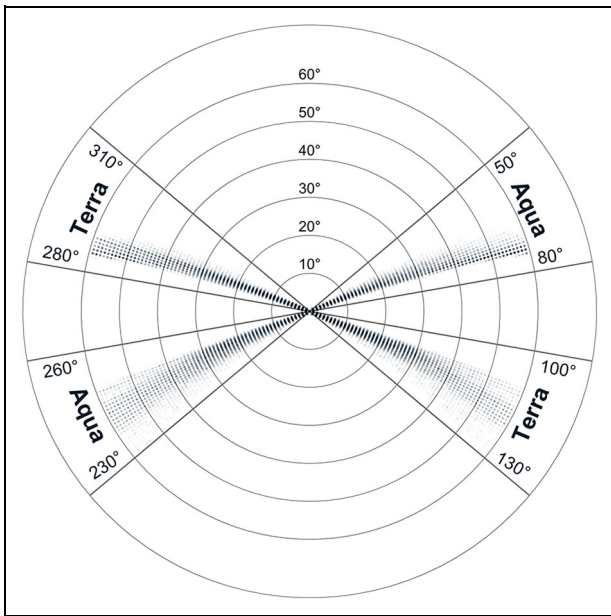


**Figure 2. Typical Arctic satellite viewing geometries for MODIS Aqua and Terra.** The centroids from sea ice concentration product of the NSDIC 25-km polar stereographic grid were used to extract approximately 100,000 surface reflectance values and associated geometries distributed over ice covered pixels for May–September of the year 2013. This information was extracted from the Application for Extracting and Exploring Analysis Ready Samples Tool (AppEEARS Team, 2018). All of the geometries were aggregated to  $1^\circ \times 1^\circ$  angular resolution bins, and the amount of surface reflectance observations within each bin was used to determine the opacity of the bins in the figure. DOI: <https://doi.org/10.1525/elementa.2020.00080.f2>

angular samples and the time for which a surface is not changing (Schaaf et al., 2011). The Arctic Ocean imposes exceptional constraints, mainly the prevalent cloud cover and the rapidly changing surface. Accordingly, we formulated an empirical model that converts each clear-sky remote sensing surface reflectance to albedo.

From a remote sensing perspective, to consider the orientation of surface roughness features was not realistic, especially as sea ice is potentially drifting around with winds and currents. Thus, Arctic sea ice surfaces, unlike ocean waves or wind-sculpted snow often found in Antarctica (Warren et al., 1998; Hudson et al., 2006), were simply assumed to be azimuthally homogeneous surfaces and, consequently, only the relative azimuth angle between the sun and the satellite was considered. Building on this assumption, we could rearrange the viewing geometries using only the relative azimuth angle with the Sun positioned at  $180^\circ$ . We observed that throughout the melt season at the northernmost latitudes both MODIS sensors have a limited domain of angular sampling (Barnsley et al., 1994; Privette et al., 1997). Over  $66.6^\circ$  N, between May and September, MODIS sweeps from across track scanning display only small variations in the azimuthal viewing geometries (Figure 2). This pattern of

viewing geometries reduces the distribution of ARF values and constrains the conversion of surface reflectance to albedo.

The solar zenith angle in the Arctic (over  $66.6^\circ$  N) is always greater than  $43^\circ$ . The angular and spectral dependence of surface reflectance is expected to increase for large solar zenith and satellite viewing zenith angles (Perovich, 1994; Bourgeois et al., 2006). Additionally, at large solar zenith or satellite viewing zenith angles (towards  $90^\circ$ ), we expect an increase in error due to a longer atmospheric path radiance and reduced at-sensor signal-to-noise ratio. For these reasons, we only examined situations with a solar zenith or satellite viewing zenith angle less than  $65^\circ$  and  $60^\circ$ , respectively. The latitudinal limitation and avoidance of long optical paths thus also constrains the ARF values.

The Arctic exhibits a complex mixture of surfaces. For practical reasons, we decomposed Arctic sea ice into discrete surface categories. Perennial sea ice has a different physical structure than first-year ice because of the summer melt (Grenfell and Maykut, 1977). It is also thicker. In view of the distinctively complex topography and limited (and decreasing) spatial coverage (Kwok et al., 2009; Comiso, 2012), we decided to focus on first-year ice, again restricting the possible ARF values. Following Perovich et al. (2002), for a simplified representation of the seasonal evolution of first-year sea ice, four dominant categories were identified: dry snow, melting snow, bare ice and melt ponds.

The operational MODIS surface reflectance product is distributed for three visible bands not saturating over sea ice. MODIS also records in six visible ocean color sensor bands, but these bands have a high sensitivity that makes them reach digital saturation over sea ice surfaces. Figure 3 shows the spectral distribution of the selected three MODIS bands in the visible range i.e. bands 01 (613–682 nm), 03 (451–481 nm) and 04 (538–569 nm). These bands are well distributed to cover the spectral range that is of interest for studying photosynthesis. Aqua and Terra sensors have very similar spectral responses (Figure 3). Thus, we assume that Terra's spectral response equals Aqua's spectral response. Overlaid are the measured albedos of snow, bare ice and melt ponds surfaces measured at Resolute Bay, Canada, from Perovich (1994). These representative spectra are added to illustrate how smooth the albedos of sea ice surfaces are over the visible range (no sharp spectral features). This smoothness supports our premise that three sensor bands should capture most of the information contained in the visible range. In fact, both the magnitude of the signal and the spectral shape of the surface carry relevant information that is used by our model. For algorithm development, we had to represent the surface reflectances of the available satellite bands by mimicking surface reflectances from high spectral resolution data (in situ and modeled; see below) scaled to the satellite spectral response functions.

So far, we have stated that a model to convert from surface reflectance into albedo should yield an albedo estimate for every surface reflectance observation. This model should be developed to be valid under specific sun

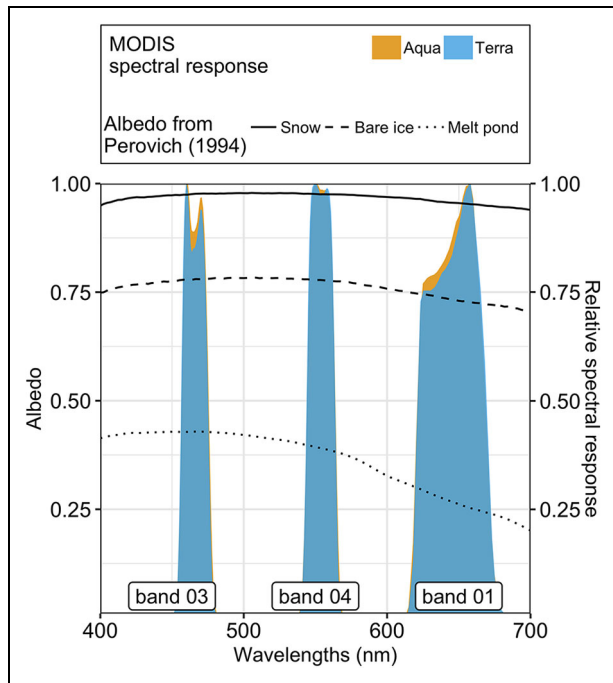


**Figure 3. MODIS spectral response.** The three MODIS visible bands and their relative spectral responses, shown with typical sea ice albedo values over the visible spectral range (400–700 nm). DOI: <https://doi.org/10.1525/elementa.2020.00080.f3>

and viewing geometries (azimuthal and zenithal), applicable to a limited number of surface categories, and based on the current satellite band availability. As with any empirical model, our model will be limited by the amount of high-quality data used to develop it, and limited Arctic sea ice data exist. Even if in situ surface reflectance generally represents a valuable ground truth, it contains measurement uncertainties due to the intrinsic complexity involved, and, for the sake of algorithm development, covers too limited a range of variations in illumination conditions and in terms of surface categories (described in Section 2.3.1). Thus, physical descriptions of sea ice reported in the literature for our typical surface categories were used to compute a more diverse synthetic sea ice surface reflectance dataset simulated through a radiative transfer model (described in Section 2.3.2).

**2.3. Data**

In this section, we first present the data used to develop our algorithm. We used in situ surface reflectance because, unlike models, in situ data have no chance of suffering from possible errors in computer programs or from the possible omission of the relevant physics. We used models because they are immune from possible uncertainties on calibration, temperature variations, gain or roll-off. A combination of both leverages their advantages and diminishes their weaknesses. We also present an independent in situ dataset that will be used to evaluate our model, as well as the remote sensing surface reflectance that will be input to the algorithm, namely the operational MODIS surface reflectance product. Finally, we

present a set of ancillary data from a specific site that helps to verify if the PAR albedo presents realistic values when derived from remote sensing data.

The Green Edge field campaign took place at a fixed location on landfast first-year ice in Western Baffin Bay (67°28' N, 63°48' E; **Figure 4** inset) near Qikiqtarjuaq along the east coast of Baffin Island, Canada. This area is where we will demonstrate the ability of the model to predict albedo. In consideration of the land surrounding the sampling site, we chose to define our study area as a 9-km<sup>2</sup> zone, which corresponds to 6 x 6 MODIS surface reflectance pixels as shown in **Figure 4**. The study period was from spring conditions (beginning of May, about –8°C) to ice break up (mid-July, about 10°C) for 2015 and 2016. Because the field sampling strategy was set to characterize the phytoplankton spring bloom dynamics, many light-related variables were collected on site, including key observations of in situ surface reflectance.

**2.3.1. In situ surface reflectance**

A dataset of highly resolved angular and spectral resolution field surface reflectance was derived from measurements taken during the 2015 Green Edge Campaign (Goyens et al., 2018). The complete dataset was generated using a regression analysis and includes:

1. measurements from a camera of hyperangular resolution (CamLum; Antoine et al., 2013) of 16,020 quadrilateral regions of uniform flux ratios at 1° resolution in  $\theta$  and at 2° resolution in  $\phi$  over the upper hemisphere;
2. measurements from a field spectroradiometer (Analytical Spectral Device) of hyperspectral resolution subsampled to give contiguous wavelength bands of 5 nm between 400 and 700 nm; and
3. three typical Arctic surface types measured under similar sun zenith angles, namely, dry snow (sun zenithal angle at 56°), bare ice (sun zenithal angle at 60°) and melt ponds (sun zenithal angle at 57°).

Full description of the method used to generate the dataset can be found in Goyens et al. (2018) and is available online (Massicotte et al., 2020). In brief, a multispectral circular fish-eye radiance camera (measuring radiances simultaneously in all directions) was combined to a hyperspectral field spectroradiometer guided by a metal arch (measuring surface leaving radiances successively with a goniometer for the angular increments). These in situ surface reflectances were scaled with the MODIS spectral response function (<https://mcst.gsfc.nasa.gov/>) to obtain three weighted band averages (Equation 2). To filter out part of the fine-scale irregular features emerging from a limited sample size (less relevant to a general solution for Arctic scale satellite remote sensing), the dataset was resampled to coarser 10° x 15° angular bins.

Viewing zenithal angles were limited to  $\leq 60^\circ$ . Towards larger angles, contamination from surrounding surfaces is hard to prevent. The lack of large viewing zenithal angles

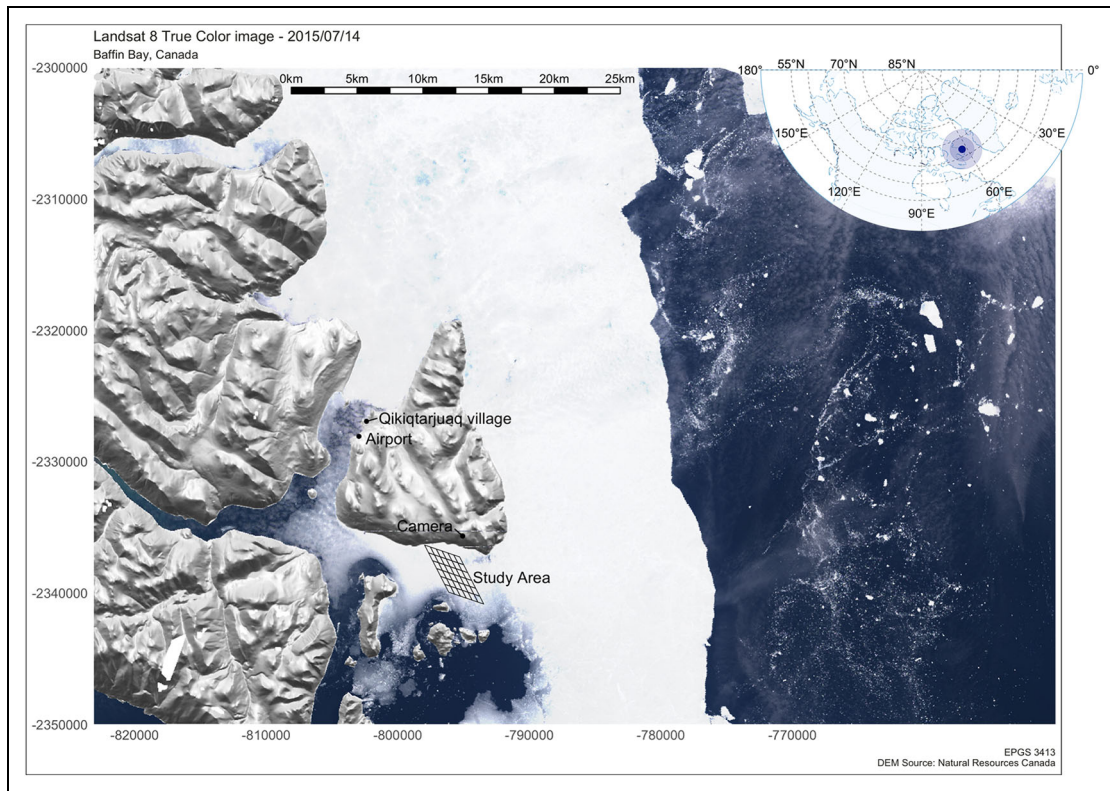


**Figure 4. Green Edge study area.** The study area is shown by the 36 MODIS 500-m pixels superimposed onto a Landsat (30-m spatial resolution) true color image from USGS on July 14, 2015, and land relief from Natural Resources Canada (computed from a 5-m spatial resolution digital elevation model). The sea ice margin is visible to the right of the image. The 25-km scale bar shows the typical spatial resolution of scattermeters and passive microwave radiometers. Inset shows the image location in the Arctic. DOI: <https://doi.org/10.1525/elementa.2020.00080.f4>

in the goniometer/camera-based dataset from Goyens et al. (2018) precluded the computation of the true albedo from surface reflectances (Equation 3). Given that the contribution of radiance at viewing zenith angles below  $60^\circ$  accounts for 75% of upward irradiance, the computed albedo from this dataset is in reality an approximation of the albedo. A total of three albedo values were computed from the in situ data.

### 2.3.2. Simulated surface reflectance

Simulated surface reflectances from radiative transfer simulations were used to reproduce several environmental conditions. Complementing the in situ data, they were also used to train our algorithm as they simultaneously provide both the surface reflectances and the PAR albedo. Assuming that the atmosphere-sea ice-ocean system is sufficiently horizontally homogeneous, AccuRT (Hamre et al., 2017; Stamnes et al., 2018) should be a suitable radiative transfer tool for simulation of various sea ice surface reflectances, as it is built on the well tested and extensively used discrete-ordinate radiative transfer method DISORT (Stamnes et al., 1988), which has been developed to handle media of different refractive indices (Jin and Stamnes, 1994), with additional development of parameterizations of atmosphere, snow, sea ice, and ocean inherent optical properties (Hamre et al., 2004; Stamnes et al., 2011; 2018).

The fully coupled atmosphere-sea ice model was used to run 36 simulations (with 64 streams) over the visible range at 5-nm spectral resolution, with  $10^\circ$  angle resolution in  $\theta$ ,  $15^\circ$  resolution in  $\phi$ , and all four surface types. The upwelling radiances are resolved at non-equal-area quadrilateral regions of constant fluxes over a hemisphere of  $2\pi$  (surface and sky domes). We computed the downward and upward irradiances above the surface, and the upward radiances from  $0$  to  $90^\circ$  in  $\theta$  and  $0$  to  $360^\circ$  in  $\phi$ , to derive an equivalent physical quantity to what is provided by the MODIS surface reflectance product. These synthetic, hyperspectral simulated surface reflectance values were also scaled by the MODIS spectral response function.

The rationale was to represent these four distinct categories (dry snow, melting snow, bare ice, and melt ponds) under natural illuminations and typical physical variations. Three sun zenithal angles ( $45^\circ$ ,  $55^\circ$  and  $65^\circ$ ) were chosen to be representative of relevant satellite observations for reasons established in the previous section. An oceanic aerosol model was used (Ahmad et al., 2010; IOCCG report, 2015). For each snow and ice medium, two layers were present. Realistic sea ice physical values were obtained from Light et al. (2003), Hamre et al. (2004), Marks and King (2014), Taskjell et al. (2017) and Oziel et al. (2019). The main features of the simulations are summarized as follows. For the dry and melting snow cases, the fine and coarse (respectively) geometrical thickness of the snow grain layer was changed from large to small

(0.10 m, 0.05 m and 0.025 m) and overlaid by a constant 0.01-m layer of fresher snow, covering the transition at the melt onset. This approach resulted in a transitional decrease in the portion of light scattered upward (Warren, 2019). The main characteristic for the dry snow case is the presence of a snow with a density of  $320 \text{ kg m}^{-3}$  and an effective snow grain radius of  $300 \mu\text{m}$ . The snow in the melting snow case had the same thickness but a density of  $400 \text{ kg m}^{-3}$  and an effective grain radius of  $1000 \mu\text{m}$ . For the bare ice, the ice thickness was changed from thicker to thinner (0.95 m, 0.50 m and 0.30 m). On top, a surface scattering layer of 0.02 m was assumed. The surface scattering layer (here represented by old snow) had a density of  $500 \text{ kg m}^{-3}$  and an effective grain radius of  $1200 \mu\text{m}$ . This top layer was meant to dominate the scattering budget so that little variation in the reflected light was observed (Perovich, 2005). Finally, for the 0.10-m deep melt ponds, ice thickness was varied (0.95, 0.50 and 0.30 m) because the light reflectance depends very little on water thickness (Makhtas and Podgorny, 1996).

### 2.3.3. Evaluation dataset of surface reflectance

We used in situ and simulated surface reflectances to train our model, but it was desirable to have an additional collection of independently measured surface reflectances of sea ice to evaluate the performance of our model. Perovich (1994) examined five cases of first-year sea ice with a hyperspectral spectroradiometer guided by a goniometer at Resolute, in the Canadian Archipelago. The objective for making these field observations was to help with the interpretation and application of directional satellite measurements made over a variety of ice conditions. During the melting season, surface reflectance and corresponding albedo measurements were performed over dry snow, snow with a glazed surface (glazed snow), bare ice, blue ice and melt ponds. Each surface type was assessed by a single set of scans with a sun zenithal angle around  $58^\circ$  (see table 1 in Perovich, 1994). Measurements for the viewing geometry were made from  $0$  to  $60^\circ$  with  $10^\circ$  increments in  $\theta$  and from  $0$  to  $360^\circ$  with  $30^\circ$  increments in  $\phi$ . As formulated above, only the restricted zenithal viewing angles and MODIS-specific azimuthal range were of interest to us for the evaluation (Section 2.2; **Figure 2**). Because the irradiances and PAR albedo were not included in the dataset, the PAR albedo could not be computed with Equation 4, but it was approximated by the mean of the spectrally resolved albedo measurements of the visible interval (approximately 3-nm spectral resolution; shown in **Figure 3**). Using the simulated surface reflectances, we compared this approximation with the values derived from Equation 4 and found the approximation to be a reasonable assumption.

Since we are mostly interested in the performance of the model when applied to remote sensing data, we also used this evaluation dataset to assess the impact of atmospheric corrections. In theory, the remote sensing surface reflectance is corrected for atmospheric scattering and absorption and is supposed to represent what would be measured directly in the field (see next section), but this

process is non-trivial. In fact, the level of accuracy of the atmospheric corrections for the surface remote sensing reflectance product is estimated to be typically  $\pm 0.005 + 5\% * \text{surface reflectance}$  (Vermote et al., 2015). Using that range as an imperfect estimate of uncertainty for surface reflectance, represented as a 99% confidence interval under the assumption that this error is normally distributed, we propagated the atmospheric correction uncertainties in the evaluation dataset of surface reflectance and estimated the resulting uncertainty in the albedo estimates.

We compared the predicted PAR albedo ( $M_i$ ) to the observed PAR albedo ( $O_i$ ) and computed the mean absolute error (MAE; Equation 5), the root mean square error (RMSE; Equation 6) and coefficient of determination ( $R^2$ ) metrics.

$$MAE = \frac{\sum_{i=1}^n |M_i - O_i|}{n} \quad (5)$$

$$RMSE = \sqrt{\frac{\sum_{i=1}^n (M_i - O_i)^2}{n}} \quad (6)$$

These metrics were chosen for their simplicity and different representativeness of the distribution of error in the model. Both Equations 5 and 6 present average error metrics in the same units as the PAR albedo, with the RMSE being more sensitive to outliers. The coefficient of determination represents the variation in the measured PAR albedo that is explained by our predictive model and is unitless.

### 2.3.4. Remote sensing surface reflectance

The MODIS surface reflectance level 2G-Lite daily products (Aqua MYD09GA and Terra MOD09GA) include three 500-m spatial resolution visible bands (introduced in **Figure 3**). These geophysical products are corrected for the effects of atmospheric scattering (aerosols, thin cirrus clouds) and absorption (aerosols, ozone and water vapor) and thus aim to represent instantaneous estimates of surface reflectance that would be measured at the Arctic surface. In other words, the numerical values derived from remote sensing are meant to have the same physical meaning (SREF; Equation 1) than our in situ surface reflectance (Section 2.3.1), simulated surface reflectance (Section 2.3.2) and evaluation dataset of surface reflectance (Section 2.3.3).

We considered only the best quality satellite observations, defined as follows: 1) cloud masking was performed by MODIS MOD35 product in addition to the surface reflectance product internal cloud algorithm; 2) values flagged as none-high band quality (see Vermote et al., 2015, their table 10) were discarded; and 3) pixels with presumed cloud shadow or high aerosol loads, or having sun zenithal angles  $> 65^\circ$  and viewing zenithal angles  $> 60^\circ$ , were removed. Note that the in situ data (Section 2.3.1) were acquired with sun zenithal angles around  $60^\circ$  but the simulated data (Section 2.3.2) extended to sun zenithal angles of  $65^\circ$ , which makes us confident our

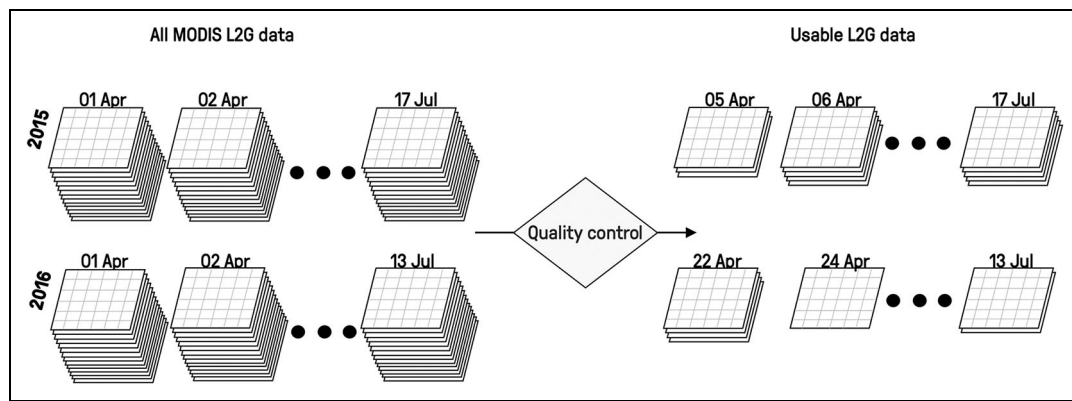


**Figure 5. The MODIS surface reflectance quality control.** The product L2G format preserves all the observational data (up to 14 per day for the Green Edge study area). Every  $6 \times 6$  pixel grid (left of the figure) is referring to the gridded area depicted in **Figure 4** but stacked to represent the 14 satellite passes collected over a single day. Surface reflectance values, quality indicators and associated sun-satellite geometry are embedded in each pixel. The quality control which includes the removal of cloudy scenes, highly reduces the amount of remote sensing surface reflectances that will be converted to albedo (right side of the figure). DOI: <https://doi.org/10.1525/elementa.2020.00080.f5>

algorithm can process satellite-derived surface reflectance with sun zenithal angles  $< 65^\circ$ .

Combining Aqua and Terra sweeps across the viewing hemisphere regularly provides up to 14 observations of the Green Edge study area per day (**Figure 1**). In this investigation we used all satellite passes (layers), regularly yielding multiple individual viewing and illumination geometries in a single day (**Figure 2**). To derive area-averaged seasonal time series of PAR albedo over the study area, we used a  $6 \times 6$  pixel spatial window of Aqua and Terra daily surface reflectance products centered on the Green Edge study area (**Figures 4** and **5**). Satellite passes were retained if, within the spatial window, they contained more than three valid pixels. Pixels were retained if, within an entire day, they had a coefficient of variation (standard deviation divided by the mean) less than or equal to 25% for the surface reflectance values of each band.

### 2.3.5. Ancillary data

Other variables were compiled to provide a context for local PAR albedo fluctuations. For the Green Edge study area, spectral albedo data were acquired on site in the spring of both years (i.e., 2015 and 2016; Verin et al., 2019). SOLALB (a custom-built radiometer) measurements at 3-nm spectral resolution (Picard et al., 2016) were collected at random locations over the study area every second day using a metallic arm at 0.80 m above the surface. Integration times were automatically adjusted for the 10 spectra acquired in triplicate at each site (snow pits and transects, 5-m intervals over 100 m to 150 m). Daily averages of PAR albedo were computed from this dataset. Melt pond fraction was derived using a time-lapse of photographs taken from a high vantage point North of the study area (surrounding hill of elevation approximately 310 m; **Figure 4**). Melt pond fraction at the ice camp was derived based on a classification similar to that used by Perovich et al. (2002), Katlein et al. (2015), and Taskjelle et al. (2017). All

photos (30-min temporal resolution, daylight) with a clear near-surface atmosphere were RGB-transformed and cropped to cover approximately the  $9 \text{ km}^2$  area of interest. A fixed threshold of 0.5 in RGB intensity was chosen to distinguish melt ponds from bare ice. Melt pond fraction was averaged every second day and interpolated to obtain daily values. Finally, rain and snow precipitation data were summarized from hourly to daily from Qikiqtarjuaq airport (**Figure 4**) located 12 km away (provided by Environment and Climate Change Canada).

### 2.4. Predictive model

Altogether, the in situ (Section 2.3.1) and simulated datasets (Section 2.3.2) cover a large array of sea ice surface reflectances and corresponding PAR albedos. This dataset was used to train a model that converts remote sensing surface reflectances (Section 2.3.4) to PAR albedo. The technical details of the model are presented here.

First, a time series of  $n$  remote sensing data was retrieved and added to the training dataset to form a single matrix. This matrix has seven columns: surface reflectance in band 03 ( $SREF_3$ ), surface reflectance in band 04 ( $SREF_4$ ), surface reflectance in band 01 ( $SREF_1$ ), sun zenithal angle ( $\theta_i$ ), viewing zenithal angle ( $\theta_v$ ), relative azimuthal angle ( $\Delta\phi$ ) and PAR albedo ( $\alpha_{PAR}$ ). It has a total of  $m$  rows, with  $k$  rows from the training data and  $n$  rows from remote sensing data ( $m = k + n$ ). At this point, the PAR albedo is not available for the  $n$  rows from remote sensing data. Second, we selected only the six columns representing the three surface reflectance bands and their three geometrical configurations. This subset matrix has the dimensions of  $m \times 6$ . We centered and scaled the subset matrix and computed its principal components. In the new coordinate system, the  $m$  rows are representing the scores of the six principal components. Third, the first  $k$  rows of the scores (associated to the training data) were regressed against the known PAR albedo to



form a multilinear regression with seven coefficients (one intercept,  $B_0$ , and six coefficients,  $B_{w=1, \dots, 6}$ ). To avoid overfitting the data, a subset of the coefficients was selected with a stepwise regression process based on the Akaike information criteria (Akaike, 1973). Fourth, the predictive model of the form

$$\alpha_{PAR}^q = B_0 + \sum_{w=1}^{\leq 6} B_w \cdot PC_w^q \quad (7)$$

was used to map the unknown PAR albedo ( $\alpha_{PAR}^q$ ) for the remaining scores ( $PC_w^q$ ). A single observation ( $q = 1, \dots, n$ ) can represent more than a single surface category, such as bare ice and melt ponds. The predictive model can be applied to linear mixtures of the represented cases used for the development of the model. However, the model will likely be making unreliable predictions for the cases outside of the scope for which it was developed. Accordingly, we rejected any inversion made from Equation 7 that would fall outside the range [0.2, 0.98] (i.e., possibility of open water and unrealistically high values).

All instantaneous visible albedo estimates ( $\alpha_{PAR}^q$ ) were then converted to a reference instantaneous albedo at a sun zenith angle of  $\theta_0 = 65^\circ$ , so that differences in albedos are ascribable to different atmospheric or surface conditions and not to different times and latitudes. Following Lindsay and Rothrock (1994), a normalization factor based on the function  $b(\theta)$  was used as

$$\alpha(\theta_0) = \alpha(\theta) \left( \frac{b(\theta_0)}{b(\theta)} \right) \quad (8)$$

with

$$b(\theta) = 0.73 - 0.14 \cos \theta \quad (9)$$

such that  $b(\theta_0) \approx 0.67$ . In our work frame,  $65^\circ$  is the maximum sun zenith angle and the normalization factor equals one. However, this normalization factor can increase the albedo up to 7% of its original value, should the observation be made at the minimum sun zenith angle of  $43^\circ$ .

### 3. Results and discussion

#### 3.1. Details of the model

In this section we present details of the data that were used to build our predictive model.

##### 3.1.1. Variability in the albedo of sea ice

We first consider the albedo spectra gathered to train our model to convert different types of Arctic first-year sea ice surface reflectances.

Albedo spectra derived from in situ measurements (dotted lines in **Figure 6**) differ slightly from those derived from radiative transfer simulations (solid lines in **Figure 6**). In the different groups of simulated albedos, variations of the sun zenithal angle and thickness (dry snow thickness, melting snow thickness, bare ice thickness and melt pond thickness) creates the spread between the different lines. Most simulated albedo spectra agree well with measurements found in the literature. For example, snow and melting snow are similar to those found in Grenfell and Maykut (1977) in their figure 1. With snow metamorphism, snow grain size increases, the optical path increases and the albedo decreases with

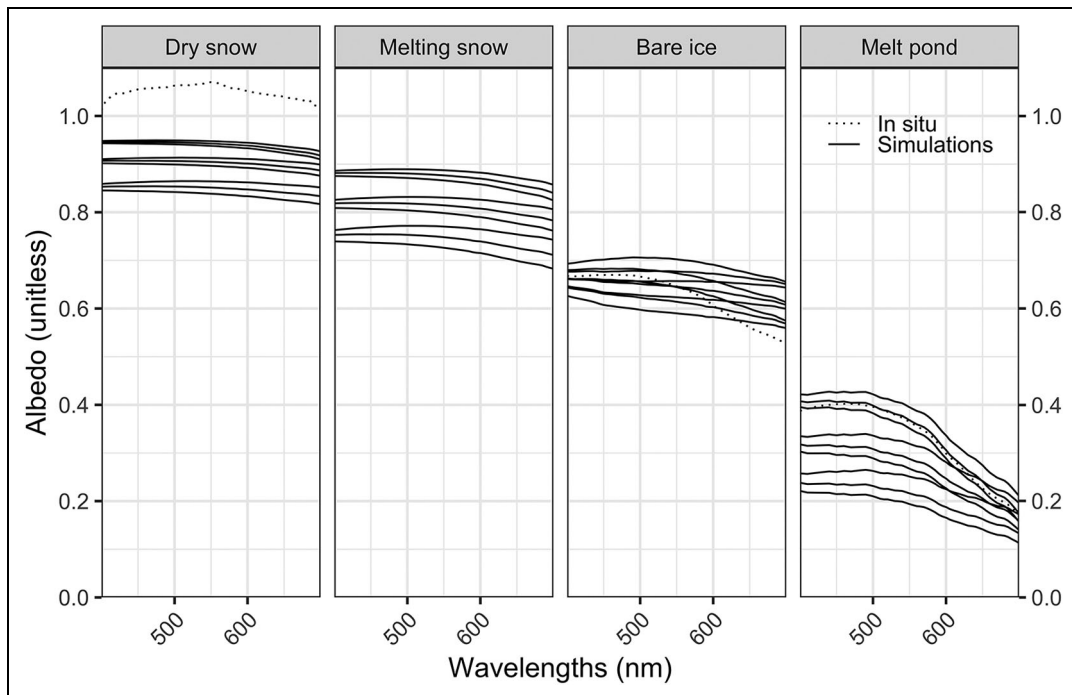


**Figure 6. All albedo values used to train our model.** Dotted and solid lines representing in situ derived (3) and simulated albedo spectra (36) for Arctic first-year sea ice, respectively. There were no in situ data for the melting snow. DOI: <https://doi.org/10.1525/elementa.2020.00080.f6>

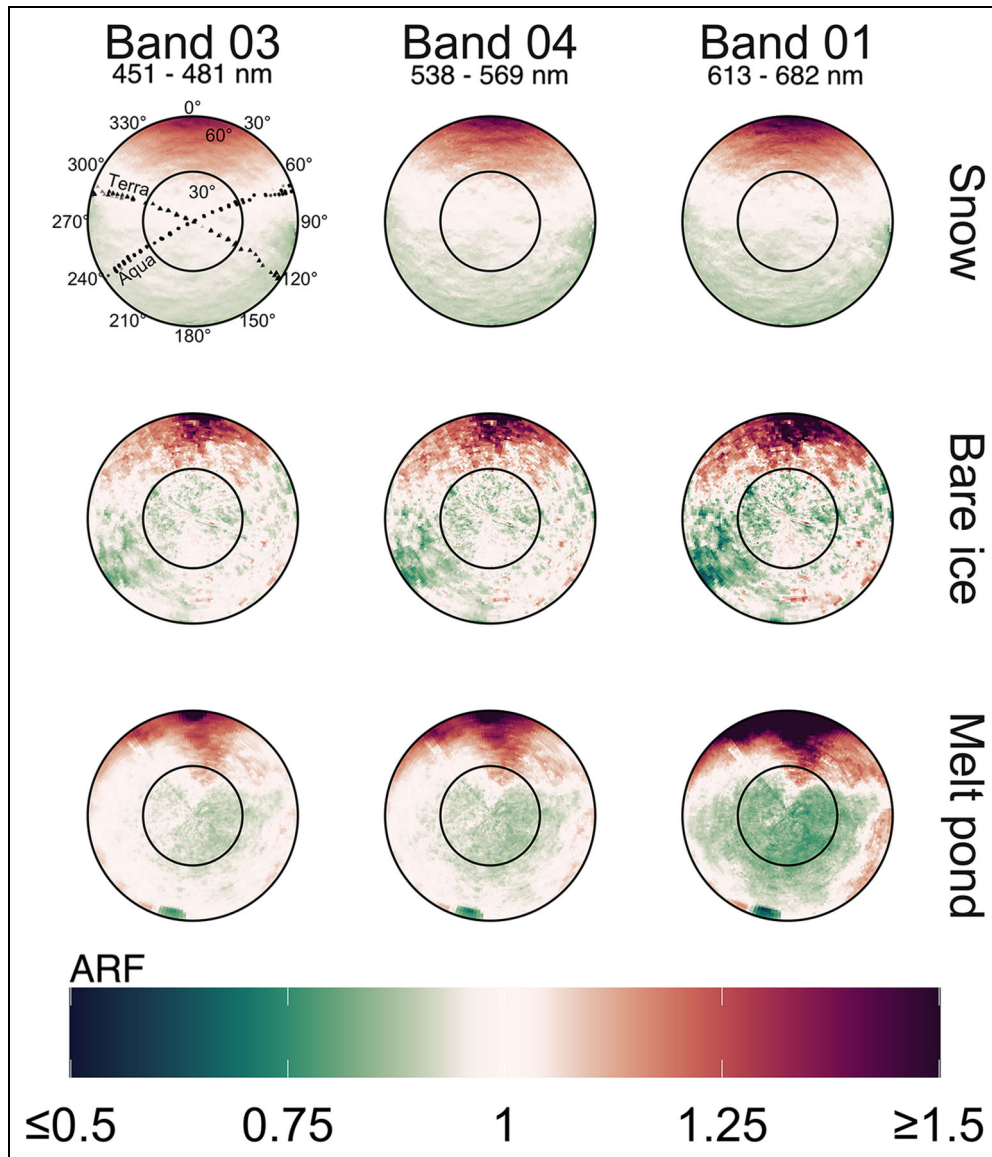


**Figure 7. In situ anisotropy reflectance factor (ARF) polar plots.** The full angular resolution from measurements of three contrasted surface types and the three MODIS bands are shown. Viewing azimuthal ( $0^{\circ}$  to  $360^{\circ}$ ) and zenithal ( $0^{\circ}$  to  $60^{\circ}$ ) angles are shown on a single plot, along with the black dots representing all MODIS Aqua and Terra viewing geometries for the Green Edge study area over the 2015 and 2016 periods studied (see **Figure 2**). The common ARF color scale diverging palette allows seeing where the isotropic assumption underestimates (green) or overestimates (red) PAR albedo. All sun zenithal angles were close to  $57^{\circ}$ ; see Section 2.3.1 for additional description. DOI: <https://doi.org/10.1525/elementa.2020.00080.f7>

time (e.g., Wiscombe and Warren, 1980). When the snow depth decreases, the underlying darker ice becomes apparent. Albedo increases with solar zenithal angle as the probability that a photon is scattered out increases when traveling at an angle close to that of the surface plane. Bare ice and melt ponds albedo are very similar to spectral albedos presented by Light et al. (2015) in their figure 4. Bare ice albedo decreases with decreasing underlying ice thickness, with the influence of underlying ice and seawater remaining minimal because of the ice surface scattering layer (Light et al., 2008). Even if the magnitudes of the bare ice spectra are generally comparable, there is a difference in spectral shape between in situ and modeled albedos, which is potentially due to

a difference in amounts of impurities. Melt pond albedo decreases with decreasing underlying ice thickness (the ocean becomes increasingly apparent). Bare ice albedo and melt pond albedo have the smallest and the greatest albedo variability in the dataset, respectively. Overall, our simulated sea ice visible PAR albedo ranges between 0.95 and 0.2.

### 3.1.2. Variability in the anisotropy reflectance factor of sea ice

The ARF values derived from in situ surface reflectance for the three surface types and three MODIS spectral bands are shown in **Figure 7**. In these and all other polar plots presented in this paper, a common azimuthal reference

has been adopted, with the viewing azimuthal angle pointing towards the Sun at  $0^\circ$ , and therefore the Sun is positioned at  $180^\circ$ . This azimuthal direction will be referred to as the principal plane, and the direction between  $90^\circ$  and  $270^\circ$  will be the perpendicular plane.

For all surface types, the largest in situ ARF values were observed in the upper part of the plots (viewing angle pointing towards the Sun). More generally, deviations from isotropy were more prominent along the principal plane while the view angles close to the perpendicular plane were more stable. The snow-covered surface showed smooth angular variations in ARF values for all bands. A notable feature was that within the circle circumscribing the  $30^\circ$  view angle (near-nadir viewing geometry), the variations were minimal and the snow ARF values were close to one. Despite more heterogeneous angular variations (speckles), which are typical of such surfaces, bare ice and melt ponds showed similar angular patterns, again with the maximum ARF values recorded when the viewing angle was pointing towards the Sun direction. A mixture of thawed ice and highly reflective ice grains caused this small-scale heterogeneity (see figure 4 in Goyens et al., 2018). The more extreme angular dependence found for bare ice and melt ponds resulted from fewer scattering events (Coackley, 2003) and internal reflections (Jiang et al., 2005; Smedley et al., 2020). For bare ice, the lower left and the lower right parts of the polar plot differ because of non-uniformly distributed fine-scale surface features. Also, because melt ponds were surrounded by a porous surface scattering layer, slightly higher ARF values were observed all around at the higher viewing zenith angles. All of these measurements are demonstrably more heterogeneous than what is typically computed from models with similar sea ice optical properties but with a surface that is perfectly homogeneous (Hudson et al., 2006). We suspect that this heterogeneity would be averaged out if the number of sites for data collection were increased.

For the ice medium, the spectral dependence of scattering in the visible wavelength interval is negligible and the absorption coefficient increases almost log-linearly with the wavelength (Warren and Brandt, 2008). As a consequence, for a given illumination condition and a given surface, the mean path length of the outgoing visible light decreases with the increasing wavelength. Therefore band04 (545–565 nm) is at an intermediate stage of anisotropy between band03 (459–479 nm) and band01 (620–670 nm), with band01 as the most anisotropic one.

**Figure 8** presents the ARF values from our simulated dataset generated using the AccuRT model, showing four surface categories (dry snow, melting snow, bare ice and melt pond), for a single set of physical properties, and the medium solar zenith angle ( $55^\circ$ ).

**Figure 8** shows a similar pattern as **Figure 7**, with a prominent hotspot in the viewing direction that opposes the azimuthal sun direction. However, this time, the surface reflectances are symmetrical with respect to the solar plane. As with the in situ data, the diverging ARF values increase with sun zenithal angle, wavelength and melt progression. Within this restricted zenithal range, the peaks in melt

pond reflectance are weaker compared to that of in situ data. Although the values used for the simulations are not meant to mimic the conditions in which the in situ data were measured but rather to represent typical Arctic sea ice under additional environmental conditions, the ARF plots show comparable anisotropy patterns.

We now specifically address the range of variation in ARF that is actually relevant to the reflectance measurements made with the MODIS sensors over the Arctic Ocean. In **Figures 7** and **8**, we superimposed onto the ARF polar plots the MODIS viewing geometry observed at the Green Edge study area (largely representative of the pattern found elsewhere in Arctic; see **Figure 2**) and at any time when the sun zenith angle is less than or equal to  $65^\circ$ . Overall, the azimuthal angle ranges between  $50^\circ$  and  $80^\circ$  ( $230^\circ$  and  $260^\circ$ ) for Aqua and from  $100^\circ$  to  $130^\circ$  ( $280^\circ$  and  $310^\circ$ ) for Terra, lying closer to the perpendicular plane than the principal plane. From a practical viewpoint, this angular domain designates the range of variation in ARF that must be addressed in an effort to estimate the PAR albedo. It is much narrower than the full range of variation in ARF. The specific satellite geometric sampling avoids measuring the maximum reflection from the sun, which is centered on the forward direction ( $180^\circ$  relative azimuth angle between sun and sensor, principal plane), as a result of the prevalent forward scattering within snow and ice, and to which specular reflection is added on melt ponds.

**Figure 9a** shows the frequency distribution of in situ ARF of the snow surface for the restricted zenithal range and for the specific azimuthal range of MODIS. We defined the restricted zenithal range as all ARF values having zenith angles below  $60^\circ$  (azimuthal range  $0^\circ$  to  $360^\circ$ ). The specific azimuthal range is a subset of the restricted zenithal range corresponding only to the possible azimuthal viewing directions of MODIS-Aqua and MODIS-Terra in the Arctic. **Figure 9b** is an alternative way of viewing the slice of ARF data from the specific azimuthal range, shown as if the data overlaid by the viewing geometry in **Figure 7** had been extracted. This slice represents only the MODIS Aqua viewing geometry (single azimuthal plane) observed at the Green Edge study area, with length of the arrows as the magnitude of the ARF values.

As can be seen in **Figure 9a**, the distribution of ARF values relevant to the measurements made with the MODIS sensors (i.e., specific azimuthal range) is narrower than when all azimuthal angles are included (i.e., restricted zenithal range). This difference is especially important in consideration of the long tail at the right of the ARF value of unity represented by the vertical dashed line in **Figure 9a**. Also, although this may not always be the case, the range of ARF values displayed in **Figure 9b** has little viewing zenithal dependence. For the snow-covered ice, the viewing geometries from MODIS are showing ARF values below unity for most of the viewing zenith angles, implying that if no correction were to be applied to the satellite surface reflectances (i.e., under the assumption of isotropy), the resulting albedo would be biased low. To generalize this observation, we extracted MODIS viewing geometries on

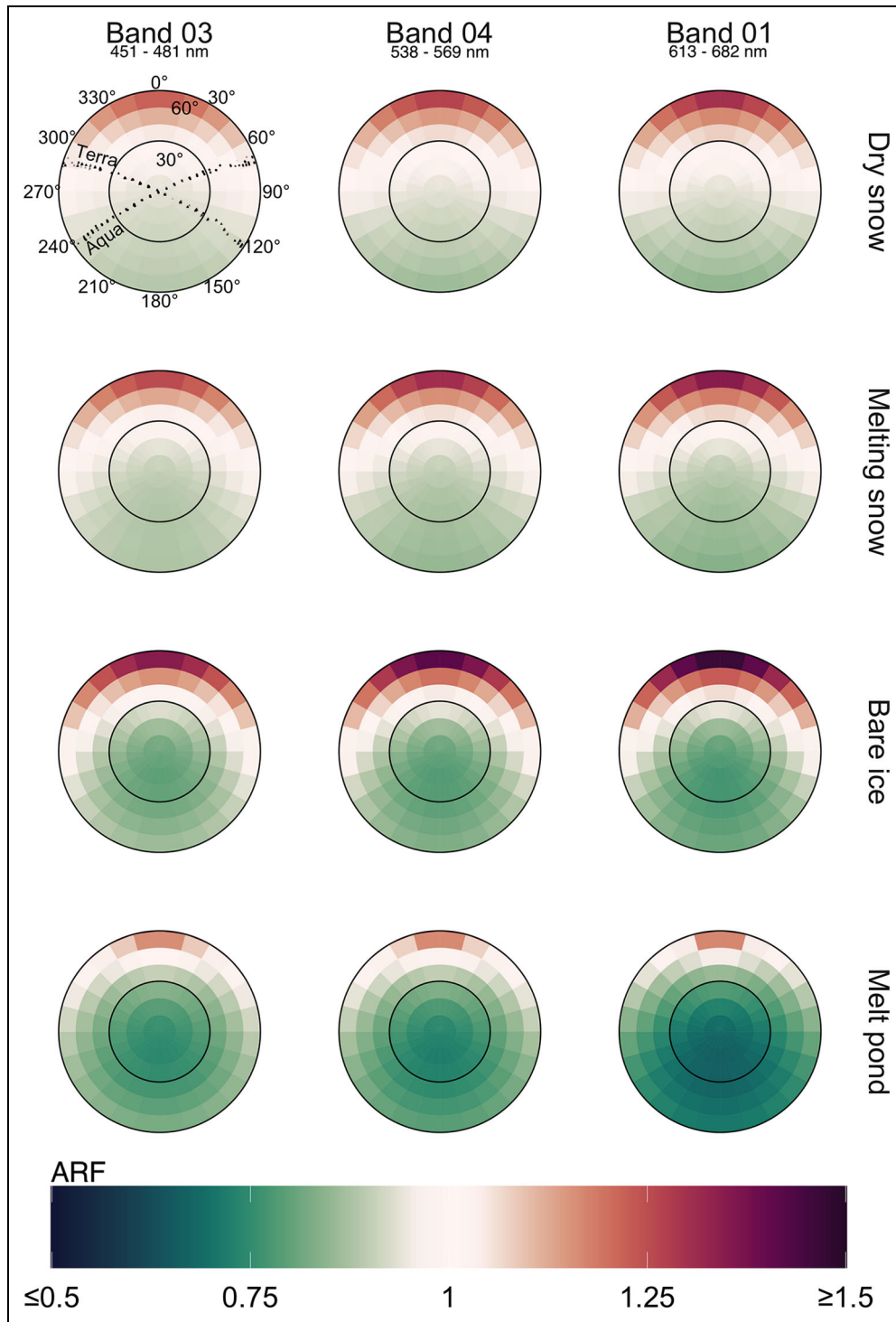


**Figure 8. Simulated anisotropy reflectance factor (ARF) polar plots.** One simulation per category is presented (Section 2.3.2), chosen to be the one with the middle of the three varying physical thicknesses with a sun zenithal angle of 55° and the zenithal viewing angle restricted to less than 60°. DOI: <https://doi.org/10.1525/elementa.2020.00080.f8>

all polar plots. In **Table 1**, we report the corresponding standard deviation of the ARF values as a measure of the spread of the distribution. We have included an additional category named all hemispheric values, which represents all ARF values within the 0° to 90° zenithal range and 0 to 360° azimuthal range.

To interpret the numbers shown in **Table 1**, consider the first block showing in situ dry snow. The middle

column, band 04, reports on the example shown in **Figure 9**. The standard deviation for the distribution of ARF of the restricted zenithal range (white histogram in **Figure 9**) is 0.08 and that of the specific azimuthal range (black histogram in **Figure 9**) is 0.04. When showing all hemispheric values, the standard deviation from the in situ dataset was removed because of the artifacts in the large angles, but computing it for the simulations was

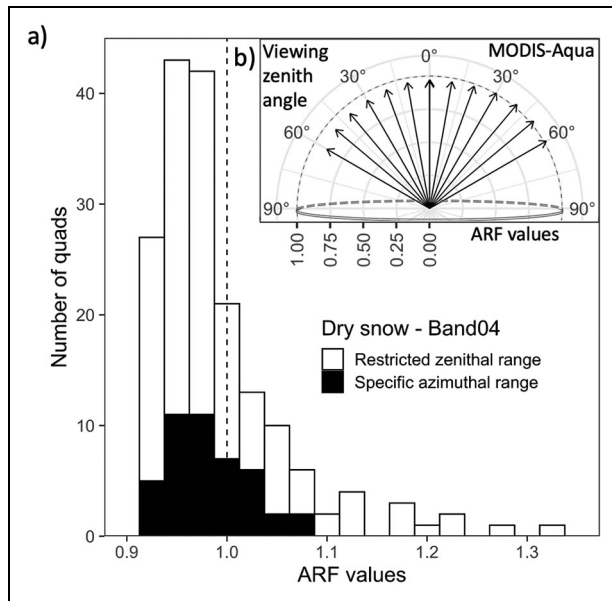


**Figure 9. Example of measured ARF values.** (a) Distribution of ARF values for in situ dry snow case in the band04 (538–569 nm) for the restricted zenith range in white (i.e., range restricted to all azimuth angles and zenith angles below  $60^\circ$ ) and for the specific azimuthal viewing range of the two MODIS sensors typical of viewing direction encountered in the Arctic (i.e., range specific to azimuthal angles between  $50^\circ$  and  $80^\circ$  and  $230^\circ$  and  $260^\circ$  for Aqua and from  $100^\circ$  to  $130^\circ$  and  $280^\circ$  and  $310^\circ$  for Terra and the zenith angles below  $60^\circ$ ). Vertical dotted line indicates ARF value of unity. (b) Display of these ARF values for the specific azimuthal range of Aqua viewing geometry, with the zenithal dependence. DOI: <https://doi.org/10.1525/elementa.2020.00080.f9>

possible. **Table 1** illustrates how restricting the viewing zenith angle to  $60^\circ$  in conjunction with MODIS-specific azimuthal range greatly reduces the spread of the ARF values for all sea ice surface types. This reduction allows for the development of a simple and robust predictive model from satellite-derived surface reflectance.

### 3.2. Evaluation of the model

Now that we have presented the spectral and angular considerations on which we base this study, we evaluate our model trained with the in situ and simulated data presented above. First, we evaluate our model directly with the 40 surface reflectances of relevant geometry and corresponding albedo from the field measurements of Perovich (1994). When compared with the corresponding field measurements of albedo, we found an MAE of 0.055, an RMSE of 0.072 and an  $R^2$  value of 0.92. The predictions are gathered around the one-to-one line, representing a good agreement with the evaluation data (**Figure 10a**). Predicting the albedo for the glazed snow and blue ice surfaces appears somewhat less accurate than for other surface types, mainly because our model was not trained for those specific surface types. Because the error metrics are hard to interpret on their own, we

used a simple model to compare the performance of our model. The averaging model does not use the angular information and computes the mean of the three bands of surface reflectances to estimate the albedo. This shortcut to derive PAR albedo from satellite data is tempting but, in principle, albedo should not be computed this way because the upward irradiances should be integrated first and then divided by the total downward irradiance. When the averaging model is used, we have an MAE of 0.085, an RMSE of 0.1, and an  $R^2$  value of 0.82. Our model outperforms the averaging model, which yields greater scatter around the desired albedo (**Figure 10b**).

Second, to evaluate the accuracy of our model when used with remote sensing surface reflectance, we added the uncertainty emerging from the correction for the overlying atmosphere. The mean (standard deviation) MAE, RMSE and  $R^2$  values were determined to be 0.057 (0.0026), 0.074 (0.004) and 0.91 (0.0071), respectively. These values represents a small decrease in performance compared with the evaluation of the dataset without the atmospheric uncertainty. The computed MAE and RMSE of the averaging model were twice as high as those of our model, and the  $R^2$  was 0.77.

Next, we use Equations 7 to 9 to derive a time series of PAR albedo from spatially and temporally neighboring surface reflectance estimates at 500-m spatial resolution between cold spring (April) and ice break up (mid-July) conditions at the Green Edge study area.

### 3.3. Albedo time series

Albedo time series were derived using the model developed above using MODIS surface reflectances for the Green Edge study area of  $6 \times 6$  pixels (approximately  $9 \text{ km}^2$ ). To create the albedo time series, our method was to average the albedo values obtained for the entire area (36 pixels) and every satellite pass in a given day. In general, within a stack as presented in **Figure 5**, possible under- and over-estimations from our model are likely to counteract one another. This regression towards the mean is an advantage of using remote sensing over high latitudes where polar orbiting satellites often revisit a given location even over a relatively short time (**Figures 1 and 5**). The mean albedo time series with the coefficient of variation (over the  $6 \times 6$  pixel area) are calculated daily and shown in **Figure 11**, along with related environmental conditions.

#### 3.3.1. Albedo and spatial heterogeneity

A comparison of satellite-derived albedo (black dots) with that derived from in situ data (open squares) is shown in **Figure 11a and e**. This comparison is not ideal for several reasons. The field data characterized an area of the order of one square meter, and the satellite data characterized the area-average properties of the non-uniform surface over several square kilometers. Moreover, no information on the time of acquisition for the in situ data was available, so normalizing to the sun position or matching data by a less-than-a-day time window was not possible. Nonetheless, even with the spatial heterogeneity of sea ice being

**Table 1.** Standard deviation of anisotropy reflectance factor (ARF) values by band of surface reflectance for the different ARF origins, cases, and types. DOI: <https://doi.org/10.1525/elementa.2020.00080.t1>

Origin	Case	Type <sup>a</sup>	Band 03	Band 04	Band 01
In situ	Dry snow	All hemispheric values	–	–	–
In situ	Dry snow	Restricted zenithal range	0.07	0.08	0.09
In situ	Dry snow	Specific azimuthal range	0.04	0.04	0.05
In situ	Bare ice	All hemispheric values	–	–	–
In situ	Bare ice	Restricted zenithal range	0.08	0.09	0.12
In situ	Bare ice	Specific azimuthal range	0.05	0.06	0.08
In situ	Melt pond	All hemispheric values	–	–	–
In situ	Melt pond	Restricted zenithal range	0.08	0.11	0.20
In situ	Melt pond	Specific azimuthal range	0.04	0.05	0.09
Simulations	Dry snow	All hemispheric values	0.21	0.25	0.28
Simulations	Dry snow	Restricted zenithal range	0.07	0.09	0.10
Simulations	Dry snow	Specific azimuthal range	0.05	0.07	0.07
Simulations	Melting snow	All hemispheric values	0.24	0.29	0.32
Simulations	Melting snow	Restricted zenithal range	0.09	0.11	0.12
Simulations	Melting snow	Specific azimuthal range	0.07	0.08	0.09
Simulations	Bare ice	All hemispheric values	0.33	0.38	0.42
Simulations	Bare ice	Restricted zenithal range	0.13	0.15	0.16
Simulations	Bare ice	Specific azimuthal range	0.10	0.11	0.12
Simulations	Melt pond	All hemispheric values	0.50	0.53	0.64
Simulations	Melt pond	Restricted zenithal range	0.11	0.12	0.13
Simulations	Melt pond	Specific azimuthal range	0.10	0.11	0.12

<sup>a</sup>All hemispheric values pertains to simulations only and refers to all ARF values within the 0° to 90° zenithal range and 0° to 360° azimuthal range; restricted zenithal range refers to values for viewing zenithal angle below 60°; specific azimuthal range refers to values for the MODIS-specific azimuthal range.

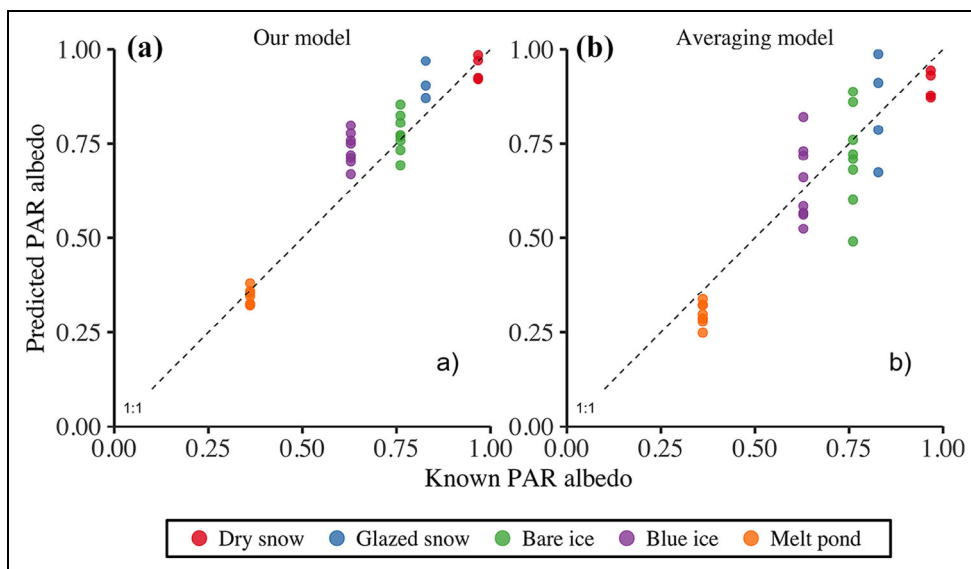


**Figure 10. Evaluation of the model.** The scatterplot shows the comparison between the albedo predicted by (a) our model and (b) the averaging model for the surface reflectances of Perovich (1994) and the known albedo from the same data set, with the dashed line as the 1:1 ratio. The color code represents the different surface categories. DOI: <https://doi.org/10.1525/elementa.2020.00080.f10>

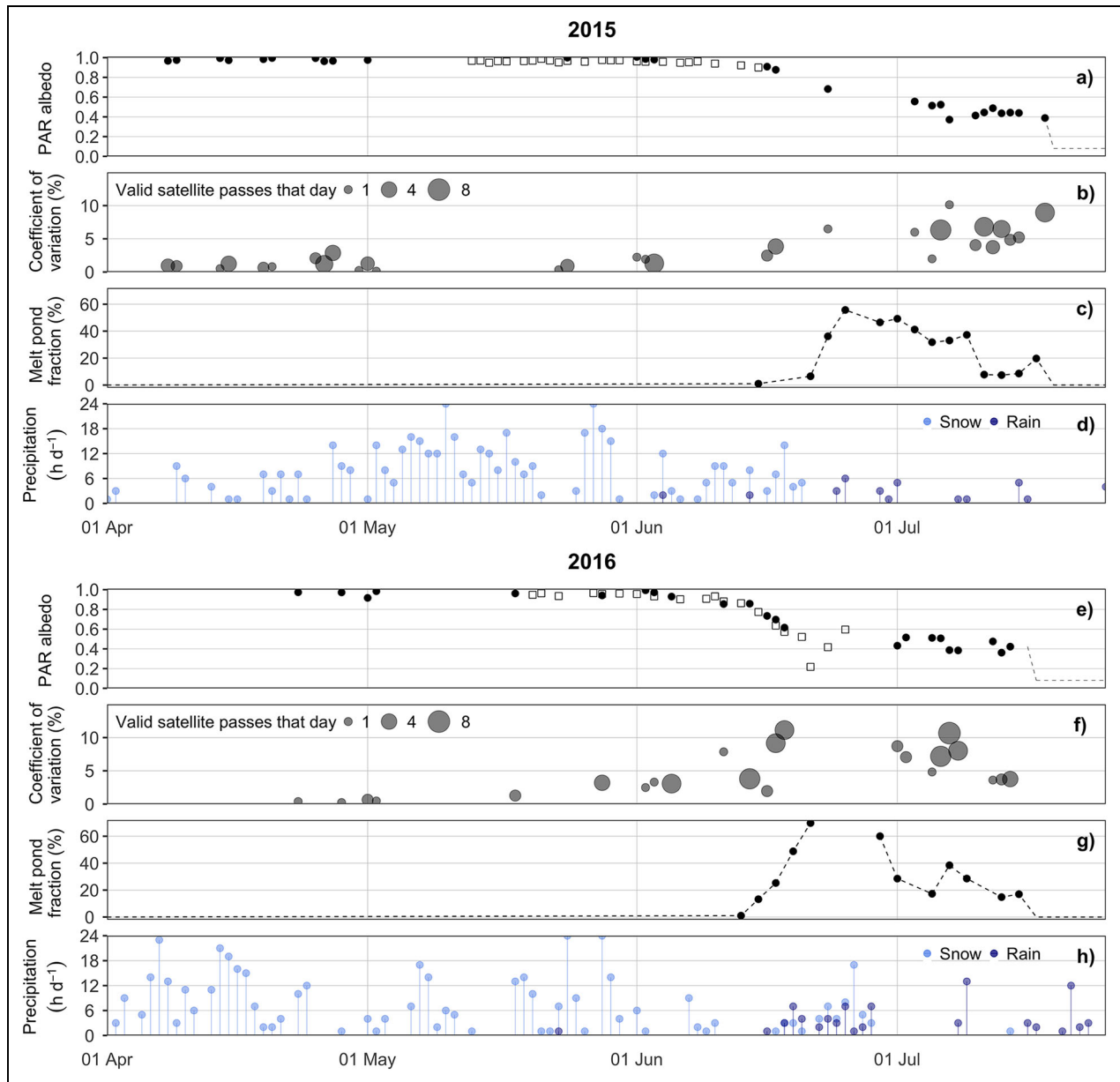


**Figure 11. Albedo, coefficient of variation, melt pond fraction, and precipitation at the Green Edge study area.** Data are shown for years 2015 and 2016. In (a) and (e), the daily PAR albedo built from instantaneous MODIS observations of surface reflectance is presented (black dots). In (b) and (f), the coefficient of variation of daily PAR albedo is presented, with dot size representing the number of valid satellite passes used to compute the daily PAR albedo. Other independently measured variables are in situ albedo (empty squares) in (a) and (e); melt pond coverage derived from photographs (black dots) in (c) and (g), with dashed lines representing the linear interpolation; and precipitation (snow and rain) in hours per day in (d) and (h) recorded at the local airport. DOI: <https://doi.org/10.1525/elementa.2020.00080.f11>

potentially quite large at sub-pixel scale (Katlein et al., 2015) and inter-pixel scale (**Figure 11b** and **f**) and the potential influence of the diurnal albedo cycle (Lindsay and Rothrock, 1994), the satellite-derived values we obtained are consistent with the albedo derived from in situ data. The comparison with in situ measurements was made, however, for periods when the spatial heterogeneity was low (i.e., when in situ data represented the areal average albedo). Nine days of measurements occurred with valid satellite retrievals (matchups) and the comparison yielded an MAE of 0.040, an RMSE of

0.043 and an  $R^2$  value of 0.96. This level of accuracy is better than what was obtained in the evaluation of the model (Section 3.2), but is only established from albedo values  $> 0.6$ , as shown in **Figure 11a** and **e**.

At the Green Edge study area over the course of the melt season, the albedo evolved similarly for years 2015 and 2016 overall (**Figure 11a** and **e**). The months of April and May exhibited relatively stable and high albedos with weak spatial heterogeneity, as expressed by the coefficient of variation calculated over the study area. In the first half of June 2015 (2016), when the surface was still very

reflective to visible radiation, the PAR albedo dropped from  $> 0.95$  to  $0.90$  ( $> 0.95$  to  $0.82$ ) and the spatial coefficient of variation increased to  $2\%$  ( $3\%$ ). Then, during the second half of June, the areally averaged PAR albedo decreased to  $0.67$  ( $0.49$ ). The spatial heterogeneity concomitantly increased reaching a coefficient of variation of  $6\%$  ( $8\%$ ) (**Figure 11b** and **f**). Finally, during the first half of July, the PAR albedo decreased to  $0.10$  for both years. The spatial heterogeneity was rather stable in July 2015 in comparison to the considerably fluctuating albedo in July 2016, with a coefficient of variation reaching  $8\%$  ( $13\%$ ) over the course of the month. This difference suggests that melt ponds were distributed more equally over the site in 2015. However, this suggestion is hard to verify because of the remarkable absence of valid satellite observations soon after the start of melt ponds due to the persistent cloud cover. For both years, the ice export due to landfast ice detachment (on July 18 in 2015; July 16 in 2016) created a drop in PAR albedo from approximately  $0.40$  to  $0.08$ , producing the most drastic change (in absolute values) in underwater light availability for phytoplankton (Lewis et al., 2019). This transition to an open water albedo defines the limit of applicability for our model.

### 3.3.2. Context variables

Context variables were chosen for their potential impact on the PAR albedo and because they were collected independently from satellite observations. There were no melt ponds prior to June 19, 2015, and June 14, 2016. The surface air temperature, measured on site by a Campbell Scientific HC2S3 temperature probe (not shown), was always below  $0^{\circ}\text{C}$  prior to May 24, 2015, and April 20, 2016, and the first day predominantly above  $0^{\circ}\text{C}$  was June 14, 2015, and May 15, 2016. Before the melt pond period, the above surface air temperature was impacting sea ice albedo, but whether variations of PAR albedo of that magnitude are ascribable to changes in temperature or simply to our inability to perfectly convert the remote sensing surface reflectances to the corresponding PAR albedo around the onset of surface melt is difficult to determine. In spite of this ambiguity, we clearly see how large variations in the independently measured melt pond fraction were captured successfully by the satellite PAR albedo time series (**Figure 11c** and **g**). The maximum recorded melt pond fractions were on June 25, 2015 ( $55\%$ ), and June 21, 2016 ( $70\%$ ). After drainage (Perovich and Polashenski, 2012), a late minimum in melt pond fraction was recorded on July 7, 2015 ( $8\%$ ) and July 4, 2016 ( $19\%$ ). Melt pond fraction increased again until ice break up ( $20\%$ ) in 2015. In 2016, it increased until July 7 ( $26\%$ ), then slowly decreased to  $16\%$  until ice break up. In the second half of June 2016, however, the intense fog prevented the camera from capturing melt pond coverage information on the surface for days. This situation is typical of the late spring and early summer in the Arctic, and clearly reveals the limitation of choosing visible imagery (including satellite remote sensing) for studying sea ice. Finally, precipitation (**Figure 11d** and **h**) should impact the PAR albedo time series enough to be captured by our method, at least when enough valid observations are available. Solid

precipitation increases the PAR albedo with fresh snow having the highest PAR albedo occurring on Earth, and liquid precipitation decreases the PAR albedo either in fostering melt and promoting metamorphism or by accumulating in melt ponds. Important snowfall events were regularly observed before mid-June of both years, keeping the PAR albedo above  $0.80$ . Snowfalls are also seen in the second half of June 2016, but because snow does not accumulate in ponds the impact was damped. The first rain events were recorded on June 4, 2015, and May 23, 2016. These short-lived and isolated episodes did not seem to affect the PAR albedo time series dramatically. However, it rained for five hours or more during three days in 2015 (June 25, July 1 and 15) and four days in 2016 (June 19, 25, 28 and July 9), and these events correspond with a period when the satellite PAR albedo time series was lower than  $0.6$ .

## 4. Conclusion and perspectives

We have shown here that achieving sea ice PAR albedo estimates over the Arctic is possible from satellite-derived surface reflectance. The main strength of our model is that it uses only the surface reflectance and associated geometry as a direct predictor of surface PAR albedo. This approach was justified by the persistent cloud cover and rapid changes occurring at the Arctic Ocean surface. Where scarcity in data availability would impede the identification of an appropriate sea ice anisotropy model, we established a conservative frame into which a predictive model can process the surface reflectances and provide a PAR albedo retrieval for every clear-sky satellite passage without using any other ancillary data.

Based on in situ measurements and the prescribed atmospheric correction uncertainty, the estimated PAR albedo had a mean absolute error of  $0.057$ , a root mean square error of  $0.074$  and an  $R^2$  value of  $0.91$ . We recognize that this model would benefit from a more extensive error analysis in the future. The surface reflectance products are processed using a mature atmospheric correction model, and quality control is indicated by a large array of quality flags of the operational processing. Yet, uncertainty estimates from Vermote et al. (2015) that we used to refine the evaluation of our model were provided as a general measure of quantitative error. An evaluation of the surface reflectance product above large expanses of landfast or mobile sea ice in different clear-sky atmospheric conditions would be appropriate, especially because atmospheric corrections in the Arctic are known to be challenging (IOCCG, 2015). In acknowledgement that absolute values are sensitive to atmospheric corrections, we tried building a model from band ratios but, on the basis of ancillary data, found that it was not evolving dynamically enough over the course of the melt season. The band ratios would also be a strong function of impurities like biogenic material, dissolved organics or sediments. Absolute surface reflectance values, along with their associated geometries, were found to contain sufficient information to investigate the dynamic seasonal evolution of albedo. Our model to derive PAR albedo is also pending proper large-scale validation. Such an exercise



would be possible by comparing satellite-retrieved values with airborne radiometric data collected near the surface. This exercise should at least be performed over sea ice at different melting stages to evaluate the full range of sea ice PAR albedo values (0.98 to 0.2).

At the moment, the model only achieves realistic PAR albedo estimates with similar sea ice conditions to those for which it was developed, that is, first-year sea ice surfaces such as dry snow, melting snow, bare ice and melt ponds (in situ and simulated surface reflectance described in Sections 2.3.1 and 2.3.2). Including more ground-based or airborne measurements of surface reflectance and corresponding albedo to train the model, providing a rigorous quality control of the data, would improve the model predictive power and broaden the scope of applicability to a wider range of sea ice conditions. In addition, having more data on sea ice physical properties and/or the inherent optical properties would facilitate the reproduction of cases of sea ice in radiative transfer models. In particular, the fragile upper boundary of sea ice is what matters most for albedo but is difficult to carry to the laboratory for optical measurements (Light et al., 2015). Efforts to study surface-most IOPs directly in the field would be useful. We did not attempt to compare modeled and measured cases because of the lack of information related to the field observations, but a rigorous comparison between AccuRT modeled reflectance and measured reflectance would be a valuable scientific inquiry, given complete sets of inherent and apparent sea ice optical properties are available. More generally, a better understanding of the combined optical properties from different Arctic sea ice types, including multi-year ice would help improve satellite-based sea ice PAR albedo monitoring.

Our model is convenient for anyone facing a tradeoff between a detailed description of the seasonal evolution of PAR sea ice albedo at high spatial resolution, and the need for efficiency when deriving an estimate of this geophysical variable from an operational standpoint over large spatial extents. Using a combination of aerial images and underwater remotely operated vehicle measurements on an ice floe in northern Fram Strait, Katlein et al. (2015) showed that under-ice light variability below the scale of the kilometer was driven more by surface albedo than by sea ice thickness, showing the need for reliable satellite-derived albedo products and time series of sea ice albedo with sub-kilometer resolution. Albedo is variable from year to year (Perovich et al., 2007) and place to place (Grenfell and Perovich, 2004), and given the spatial coefficient of variation depicted in **Figure 11** for the Green Edge study area (approximately 9 km<sup>2</sup>), clearly there is high spatial heterogeneity locally (< 9 km<sup>2</sup>) and an expectedly high variability regionally (> 9 km<sup>2</sup>). Our model can be applied to examine the variations of PAR albedo at spatial scales of 500-m or greater during the melt period for different Arctic regions. We believe the differences in PAR albedo are key to a better understanding of in situ observed contrasted regimes of sympagic and pelagic biological production. In fact, deriving PAR albedo time series of melting sea ice to contextualize biological research conducted in ice camps, oceanographic cruises, or polar

expeditions is possible. The combination of MODIS-Aqua and Terra surface reflectance product required to retrieve PAR albedo is consistent and continuous since the year 2002, offering an excellent potential to examine the light regime under sea ice (Stroeve et al., 2021). Applying our method over the remote Arctic Ocean will also support year-to-year comparisons of the rapidly evolving sea ice albedo and should thus provide new insights on the impact of the changing climate on Arctic phytoplankton phenology.

#### Data accessibility statement

Data are accessible at the Green Edge database: <http://www.obs-vlfr.fr/proof/php/GREENEDGE/greenedge.php>.

#### Acknowledgments

The authors are thankful to Eric Brossier and Christian Haas for providing the time-lapse photography and to Environment and Climate Change Canada for the meteorological observations. They are also thankful to Sadashiva Devadiga for helping with the exploitation of the moderate resolution imaging spectroradiometer (MODIS) surface reflectance level 2G-Lite products and the MODIS Teams for the distribution of satellite-derived products and to Simon Bélanger and Robert Frouin for their feedback. They gratefully acknowledge scientific and financial support of Québec-Océan. Finally, they are grateful to the editor and reviewers for their constructive comments.

#### Funding

Julien Laliberté was supported by the FRQNT and the CREATE program (NSERC). Marcel Babin was funded NSERC (05175-2014). This work was funded by the Canadian Excellence Research Chair on Remote sensing of Canada's new Arctic frontier, Canadian Space Agency Green Edge project, CNES Green Edge project (131425), Network of Centres of Excellence MEOPAR, and Observation core in remote sensing project (1-02-01-064.5). We gratefully acknowledge scientific and financial support of Québec-Océan.

#### Competing interests

The authors declare that there is no conflict of interest.

#### Author contributions

Designed and wrote the study: JL.

Helped with the satellite data and drafting of the text: ER.

Helped with the radiative transfer simulations and the writing: BH.

Collected and processed the in situ data and revised the text: GC.

Provided data and revised the text: DP.

Contributed to its conception and revise the text: MB.

Approved the submitted version for publication: All authors.

#### References

**Akaike, H.** 1973. Information theory and an extension of the maximum likelihood principle, in *Proceedings*

of the 2nd International Symposium on Information Theory. Budapest, Hungary, September 2–8. pp. 267–281.

- Antoine, D, Morel, A, Leymarie, E, Houyou, A, Gentili, B, Victori, S, Buis, JP, Buis, N, Meunier, S, Canini, M, Crozel, D, Fournie, B, Henry, P.** 2013. Underwater radiance distributions measured with miniaturized multispectral radiance cameras. *Journal of Atmospheric and Oceanic Technology* **30**: 74–95. DOI: <https://doi.org/10.1175/JTECH-D-11-00215.1>.
- AppEEARS Team.** 2018. Application for extracting and exploring analysis ready samples (AppEEARS). Ver. 2.14.2. NASA EOSDIS Land Processes Distributed Active Archive Center (LP DAAC). USGS/Earth Resources Observation and Science (EROS) Center (Sioux Falls, South Dakota, USA). <https://lpdaacsv.cr.usgs.gov/appeears>.
- Arndt, S, Nicolaus, M.** 2014. Seasonal cycle and long-term trend of solar energy fluxes through Arctic sea ice. *The Cryosphere* **8**(6): 2219–2233. DOI: <http://dx.doi.org/10.5194/tc-8-2219-2014>.
- Arrigo, KR, Perovich, DK, Pickart, RS, Brown, ZW, van Dijken, GL, Lowry, KE, Mills, MM, Palmer, MA, Balch, WM, Bahr, F, Bates, NR, Benitez-Nelson, C, Bowler, B, Brownlee, E, Ehn, JK, Frey, KE, Gargett, R, Laney, SR, Lubelczyk, L, Mathis, J, Matsuoka, A, Mitchel, BG, Moore, G WK, Ortega-Retuerta, E, Pal, S, Polashenski, CM, Reynolds, RA, Schieber, B, Sosik, HM, Stephens, M, Swift, JH.** 2012. Massive phytoplankton blooms under Arctic sea ice. *Science* **336**(6087): 1408. DOI: <http://dx.doi.org/10.1126/science.1215065>.
- Arrigo, KR, Perovich, DK, Pickart, RS, Brown, ZW, van Dijken, GL, Lowry, KE, Mills, MM, Palmer, MA, Balch, WM, Bates, NR, Benitez-Nelson, CR, Bownlee, E, Frey, KE, Laney, SR, Mathis, J, Matsuoka, A, Greg Mitchell, A, Moore, GWK, Reynolds, RA, Sosik, HM, Swift, JH.** 2014. Phytoplankton blooms beneath the sea ice in the Chukchi Sea. *Deep Sea Research Part II: Topical Studies in Oceanography* **105**: 1–16. DOI: <http://dx.doi.org/10.1016/j.dsr2.2014.03.018>.
- Assmy, P, Fernández-Méndez, M, Duarte, P, Meyer, A, Randelhoff, A, Mundy, CJ, Olsen, LM, Kauko, HM, Bailey, A, Chierici, M, Cohen, L, Doulgeris, AP, Ehn, JK, Fransson, A, Gerland, S, Hop, H, Hudson, SR, Hugues, N, Itkin, P, Johnsen, G, King, JA, Koch, BP, Koenig, Z, Kwasniewski, S, Laney, SR, Nicolaus, M, Pavlov, AK, Polashenski, CM, Provost, C, Rösel, A, Sandbu, M, Spreen, G, Smedsrud, LH, Sundfjord, A, Taskjelle, T, Tatarek, A, Wiktor, J, Wagner, RM, Wold, A, Steen, H, Granskog, MA.** 2017. Leads in Arctic pack ice enable early phytoplankton blooms below snow-covered sea ice. *Scientific Reports* **7**: 40850. DOI: <http://dx.doi.org/10.1038/srep40850>.
- Barnsley, MJ, Strahler, AH, Morris, KP, Muller, JP.** 1994. Sampling the surface bidirectional reflectance distribution function (BRDF): 1. Evaluation of current and future satellite sensors. *Remote Sensing Reviews* **8**(4): 271–311. DOI: <http://dx.doi.org/10.1080/02757259409532205>.
- Bourgeois, CS, Calanca, P, Ohmura, A.** 2006. A field study of the hemispherical directional reflectance factor and spectral albedo of dry snow. *Journal of Geophysical Research: Atmospheres* **111**(D20). DOI: <http://dx.doi.org/10.1029/2006JD007296>.
- Castellani, G, Losch, M, Lange, BA, Flores, H.** 2017. Modeling Arctic sea-ice algae: Physical drivers of spatial distribution and algae phenology. *Journal of Geophysical Research: Oceans* **122**(9): 7466–7487. DOI: <http://dx.doi.org/10.1002/2017jc012828>.
- Coakley, JA.** 2003. Reflectance and albedo, surface. *Elsevier Science Encyclopedia of the Atmosphere* 1914–1923. DOI: <http://dx.doi.org/10.1016/B0-12-227090-8/00069-5>.
- Comiso, JC.** 2012. Large decadal decline of the Arctic multiyear ice cover. *Journal of Climate* **25**(4): 1176–1193. DOI: <http://dx.doi.org/10.1175/jcli-d-11-00113.1>.
- DeAbreu, RA, Barber, DG, Misurak, K, LeDrew, EF.** 1995. Spectral albedo of snow-covered first-year and multi-year sea ice during spring melt. *Annals of Glaciology* **21**: 337–342.
- Ebert, E, Schramm, J, Curry, J.** 1995. Disposition of solar radiation in sea ice and the upper ocean. *Journal of Geophysical Research: Oceans* **100**(C8): 15965–15975. DOI: <http://dx.doi.org/10.1029/95JC01672>.
- Fortier, M, Fortier, L, Michel, C, Legendre, L.** 2002. Climatic and biological forcing of the vertical flux of biogenic particles under seasonal Arctic sea ice. *Marine Ecology Progress Series* **225**: 1–16. DOI: <http://dx.doi.org/10.3354/meps225001>.
- Goyens, C, Marty, S, Leymarie, E, Antoine, D, Babin, M, Bélanger, S.** 2018. High angular resolution measurements of the anisotropy of reflectance of sea ice and snow. *Earth and Space Science* **5**(1): 30–47. DOI: <http://dx.doi.org/10.1002/2017ea000332>.
- Grenfell, TC, Maykut, GA.** 1977. The optical properties of ice and snow in the Arctic Basin. *Journal of Glaciology* **18**(80): 445–463.
- Grenfell, TC, Perovich, DK.** 2004. Seasonal and spatial evolution of albedo in a snow-ice-land-ocean environment. *Journal of Geophysical Research* **109**(C1). DOI: <http://dx.doi.org/10.1029/2003jc001866>.
- Grenfell, TC, Perovich, DK.** 2008. Incident spectral irradiance in the Arctic Basin during the summer and fall. *Journal of Geophysical Research: Atmospheres* **113**(D12). DOI: <http://dx.doi.org/10.1029/2007JD009418>.
- Hamre, B, Stamnes, S, Stamnes, K, Stamnes, J.** 2017. AccuRT: A versatile tool for radiative transfer simulations in the coupled atmosphere-ocean system. *AIP Conference Proceedings* **1810**: 120002. DOI: <http://dx.doi.org/10.1063/1.4975576>.
- Hamre, B, Winther, JG, Gerland, S, Stamnes, J, Stamnes, K.** 2004. Modeled and measured optical transmittance of snow-covered first-year sea ice in Kongsfjorden, Svalbard. *Journal of Geophysical*

- Research* **109**(C10). DOI: <http://dx.doi.org/10.1029/2003jc001926>.
- Hill, VJ, Light, B, Steele, M, Zimmerman, RC.** 2018. Light availability and phytoplankton growth beneath Arctic sea ice: Integrating observations and modeling. *Journal of Geophysical Research: Oceans* **123**: 3651–3667. DOI: <https://doi.org/10.1029/2017JC013617>.
- Horvat, C, Jones, DR, Iams, S, Schroeder, D, Flocco, D, Feltham, D.** 2017. The frequency and extent of sub-ice phytoplankton blooms in the Arctic Ocean. *Science Advances* **3**(3): e1601191. DOI: <http://dx.doi.org/10.1126/sciadv.1601191>.
- Hudson, SR, Warren, SG, Brandt, RE, Grenfell, TC, Six, D.** 2006. Spectral bidirectional reflectance of Antarctic snow: Measurements and parameterization. *Journal of Geophysical Research* **111**(D18). DOI: <http://dx.doi.org/10.1029/2006jd007290>.
- IOCCG.** 2015. Ocean colour remote sensing in polar seas, in Babin, M, Arrigo, K, Bélanger, S, Forget, MH eds., *IOCCG Report Series, No. 16*. Dartmouth, Canada: International Ocean Colour Coordinating Group.
- Jiang, S, Stamnes, K, Li, W, Hamre, B.** 2005. Enhanced solar irradiance across the atmosphere–sea ice interface: A quantitative numerical study. *Applied Optics* **44**(13): 2613–2625. DOI: <http://dx.doi.org/10.1364/AO.44.002613>.
- Jin, Z, Stamnes, K.** 1994. Radiative transfer in nonuniformly refracting layered media: Atmosphere-ocean system. *Optical Society of America* **33**(3): 431–442. DOI: <http://dx.doi.org/10.1364/AO.33.000431>.
- Katlein, C, Arndt, S, Nicolaus, M, Perovich, DK, Jakuba, MV, Suman, S, Elliott, S, Whitcomb, LL, McFarland, CJ, Gerdes, R, Boetius, A, German, CR.** 2015. Influence of ice thickness and surface properties on light transmission through Arctic sea ice. *Journal of Geophysical Research: Oceans* **120**(9): 5932–5944. DOI: <http://dx.doi.org/10.1002/2015JC010914>.
- Key, J, Wang, X, Liu, Y, Dworak, R, Letterly A.** 2016. The AVHRR polar Pathfinder climate data records. *Remote Sensing* **8**(3): 167. DOI: <http://dx.doi.org/10.3390/rs8030167>.
- Kwok, R, Cunningham, GF, Wensnahan, M, Rigor, I, Zwally, HJ, Yi, D.** 2009. Thinning and volume loss of the Arctic Ocean sea ice cover: 2003–2008. *Journal of Geophysical Research* **114**(C7). DOI: <http://dx.doi.org/10.1029/2009jc005312>.
- Laliberté, J, Bélanger, S, Babin, M.** 2021. Seasonal and interannual variations in the propagation of photosynthetically available radiation through the Arctic atmosphere. *Elementa: Science of the Anthropocene* **9**(1): 83. DOI: <http://dx.doi.org/10.1525/elementa.2020.00083>.
- Laney, SR, Krishfield, RA, Toole, JM, Hammar, TR, Ashjian, CJ, Timmermans, ML.** 2014. Assessing algal biomass and bio-optical distributions in perennially ice-covered polar ocean ecosystems. *Polar Science* **8**(2): 73–85. DOI: <https://doi.org/10.1016/j.polar.2013.12.003>.
- Lange, BA, Flores, H, Michel, C, Beckers, JF, Bublitz, A, Casey, JA, Castellani, G, Hatam, I, Reppchen, A, Rudolph, SA, Haas, C.** 2017. Pan-Arctic sea ice-algal chl a biomass and suitable habitat are largely underestimated for multiyear ice. *Global Change Biology* **23**(11): 4581–4597. DOI: <http://dx.doi.org/10.1111/gcb.13742>.
- Lewis, KM, Arntsen, AE, Coupel, P, Joy-Warren, H, Lowry, KE, Matsuoka, A, Mills, MM, van Dijken, GL, Selz, V, Arrigo, KR.** 2019. Photoacclimation of Arctic Ocean phytoplankton to shifting light and nutrient limitation. *Limnology and Oceanography* **64**(1): 284–301. DOI: <http://dx.doi.org/10.1002/lno.11039>.
- Light, B, Grenfell, TC, Perovich, DK.** 2008. Transmission and absorption of solar radiation by Arctic sea ice during the melt season. *Journal of Geophysical Research: Oceans* **113**(C3). DOI: <http://dx.doi.org/10.1029/2006JC003977>.
- Light, B, Maykut, GA, Grenfell, TC.** 2003. Effects of temperature on the microstructure of first-year Arctic sea ice. *Journal of Geophysical Research: Oceans* **108**(C2). DOI: <http://dx.doi.org/10.1029/2001jc000887>.
- Light, B, Perovich, DK, Webster, MA, Polashenski, C, Dadic, R.** 2015. Optical properties of melting first-year Arctic sea ice. *Journal of Geophysical Research: Oceans* **120**: 7657–7675. DOI: <http://dx.doi.org/10.1002/2015JC011163>.
- Lindsay, RW, Rothrock, DA.** 1994. Arctic sea ice albedo from AVHRR. *Journal of Climate* **7**(11): 1737–1749. DOI: [http://dx.doi.org/10.1175/1520-0442\(1994\)007<1737:ASIAFA>2.0.CO;2](http://dx.doi.org/10.1175/1520-0442(1994)007<1737:ASIAFA>2.0.CO;2).
- Lowry, KE, Van Dijken, GL, Arrigo, KR.** 2014. Evidence of under-ice phytoplankton blooms in the Chukchi Sea from 1998 to 2012. *Deep Sea Research Part II: Topical Studies in Oceanography* **105**: 105–117. DOI: <http://dx.doi.org/10.1016/j.dsr2.2014.03.013>.
- Lutch, W, Schaaf, CB, Strahler, AH.** 2000. An algorithm for the retrieval of albedo from space using semiempirical BRDF models. *IEEE Transactions on Geoscience and Remote Sensing* **38**(2): 977–998. DOI: <http://dx.doi.org/10.1109/36.841980>.
- Makshtas, AP, Podgorny, IA.** 1996. Calculation of melt pond albedos on arctic sea ice. *Polar Research* **15**(1): 43–52. DOI: <http://dx.doi.org/10.3402/polar.v15i1.6635>.
- Marks, AA, King, MD.** 2014. The effect of snow/sea ice type on the response of albedo and light penetration depth (e-folding depth) to increasing black carbon. *The Cryosphere* **8**(5): 1625–1638. DOI: <http://dx.doi.org/10.5194/tc-8-1625-2014>.
- Massicotte, P, Amiraux, R, Amyot, M-P, Archambault, P, Ardyna, M, Arnaud, L, Artigue, L, Aubry, C, Ayotte, P, Bécu, G, Bélanger, S, Benner, R, Bittig, H C, Bricaud, A, Brossier, É, Bruyant, F, Chauvaud, L, Christiansen-Stowe, D, Claustre, H, Cornet-Barthaux, V, Coupel, P, Cox, C, Delaforge, A,**

- Dezutter, T, Dimier, C, Domine, F, Dufour, F, Dufresne, C, Dumont, D, Ehn, J, Else, B, Ferland, J, Forget, M-H, Fortier, L, Galí, M, Galindo, V, Gallinari, M, Garcia, N, Gérikas Ribeiro, C, Gourdal, M, Gourvil, P, Goyens, C, Grondin, P-L, Guillot, P, Guilmette, C, Houssais, M-N, Joux, F, Lacour, L, Lacour, T, Lafond, A, Lagunas, J, Lalande, C, Laliberté, J, Lambert-Girard, S, Larivière, J, Lavaud, J, LeBaron, A, Leblanc, K, Le Gall, F, Legras, J, Lemire, M, Lévasseur, M, Leymarie, E, Leynaert, A, Lopes dos Santos, A, Lourenço, A, Mah, D, Marec, C, Marie, D, Martin, N, Marty, C, Marty, S, Massé, G, Matsuoka, A, Matthes, L, Moriceau, B, Muller, P-E, Mundy, C-J, Neukermans, G, Oziel, L, Panagiotopoulos, C, Pangrazi, J-J, Picard, G, Picheral, M, Pinczon du Sel, F, Pogorzelec, N, Probert, I, Quéguiner, B, Raimbault, P, Ras, J, Rehm, E, Reimer, E, Rontani, J-F, Rysgaard, S, Saint-Béat, B, Sampei, M, Sansoulet, J, Schmechtig, C, Schmidt, S, Sempéré, R, Sévigny, C, Shen, Y, Tragin, M, Tremblay, J-É, Vaulot, D, Verin, G, Vivier, F, Vladoiu, A, Whitehead, J, Babin, M. 2020. Green Edge ice camp campaigns: Understanding the processes controlling the under-ice Arctic phytoplankton spring bloom. *Earth System Science Data* **12**(1): 151–176. DOI: <http://dx.doi.org/10.5194/essd-12-151-2020>.
- Mayot, N, Matrai, P, Ellingsen, IH, Steele, M, Johnson, K, Riser, SC, Swift, D. 2018. Assessing phytoplankton activities in the seasonal ice zone of the Greenland Sea over an annual cycle. *Journal of Geophysical Research: Oceans* **123**(11): 8004–8025. DOI: <https://doi.org/10.1029/2018JC014271>.
- Mundy, CJ, Gosselin, M, Gratton, Y, Brown, K, Galindo, V, Campbell, K, Lévasseur, M, Barber, D, Papyriakou, T, Bélanger, S. 2014. Role of environmental factors on phytoplankton bloom initiation under landfast sea ice in Resolute Passage, Canada. *Marine Ecology Progress Series* **497**: 39–49. DOI: <http://dx.doi.org/10.3354/meps10587>.
- Nicodemus, FE, Richmond, JC, Hsia, JJ, Ginsberg, WI, Limperis, T. 1977. Geometrical considerations and nomenclature for reflectance. *NBS Monograph* **160**: 4.
- Nicolaus, M, Gerland, S, Hudson, SR, Hanson, S, Haapala, J, Perovich, DK. 2010. Seasonality of spectral albedo and transmittance as observed in the Arctic Transpolar Drift in 2007. *Journal of Geophysical Research* **115**(C11). DOI: <http://dx.doi.org/10.1029/2009jc006074>.
- Oziel, L, Massicotte, P, Randelhoff, A, Ferland, J, Vladoiu, A, Lacour, L, Galindo, V, Lambert-Girard, S, Dumont, D, Cuypers, Y, Bouruet-Aubertot, P, Mundy, CJ, Ehn, J, Bécu, G, Marec, C, Forget, MH, Garcia, N, Coupel, P, Raimbault, P, Houssais, MN, Babin M. 2019. Environmental factors influencing the seasonal dynamics of spring algal blooms in and beneath sea ice in western Baffin Bay. *Elementa: Science of the Anthropocene* **7**(1): 34. DOI: <http://dx.doi.org/10.1525/elementa.372>.
- Perovich, DK. 1994. Light reflection from sea ice during the onset of melt. *Journal of Geophysical Research* **99**(C2): 3351. DOI: <http://dx.doi.org/10.1029/93jc03397>.
- Perovich, DK. 2005. On the aggregate-scale partitioning of solar radiation in Arctic sea ice during the Surface Heat Budget of the Arctic Ocean (SHEBA) field experiment. *Journal of Geophysical Research: Oceans* **110**(C3). DOI: <http://dx.doi.org/10.1029/2004JC002512>.
- Perovich, DK, Grenfell, TC, Light, B, Hobbs PV. 2002. Seasonal evolution of the albedo of multiyear Arctic sea ice. *Journal of Geophysical Research* **107**(C10). DOI: <http://dx.doi.org/10.1029/2000jc000438>.
- Perovich, DK, Nghiem, SV, Markus, T, Schweiger, A. 2007. Seasonal evolution and interannual variability of the local solar energy absorbed by the Arctic sea ice–ocean system. *Journal of Geophysical Research: Oceans* **112**(C3). DOI: <http://dx.doi.org/10.1029/2006jc003558>.
- Perovich, DK, Polashenski, C. 2012. Albedo evolution of seasonal Arctic sea ice. *Geophysical Research Letters* **39**(8). DOI: <http://dx.doi.org/10.1029/2012GL051432>.
- Picard, G, Libois, Q, Arnaud, L, Verin, G, Dumont, M. 2016. Estimation of superficial snow specific surface area from spectral albedo time-series at Dome C, Antarctica. *The Cryosphere Discussion*. DOI: <http://dx.doi.org/10.5194/tc-2015-213>.
- Pinkerton, MH, Hayward, A. 2021. Estimating variability and long-term change in sea ice primary productivity using a satellite-based light penetration index. *Journal of Marine Systems* **221**: 103576. <https://doi.org/10.1016/j.jmarsys.2021.103576>.
- Porter, C, Morin, P, Howat, I, Noh, MJ, Bates, B, Peterman, K, Keeseey, S, Schlenk, M, Gardiner, J, Tomko, K, Willis, M, Kelleher, C, Cloutier, M, Husby, E, Foga, S, Nakamura, H, Platson, M, Wethington, MJr, Williamson, C, Bauer, G, Enos, J, Arnold, G, Kramer, W, Becker, P, Doshi, A, D'Souza, C, Cummins, P, Laurier, F, Bojesen, M. 2018. “ArcticDEM”, Harvard Dataverse, V3.0, [2019-01-31]. DOI: <http://dx.doi.org/10.7910/DVN/OHHUKH>.
- Privette, JL, Eck, TF, Deering, DW. 1997. Estimating spectral albedo and nadir reflectance through inversion of simple BRDF models with AVHRR/MODIS-like data. *Journal of Geophysical Research: Atmospheres* **102**(D24): 29529–29542. DOI: <http://dx.doi.org/10.1029/97jd01215>.
- Randelhoff, A, Lacour, L, Marec, C, Leymarie, E, Lagunas, J, Xing, X, Darnis, G, Penkerch, C, Sampei, M, Fortier, L, D'Ortenzio, F, Claustre, H, Babin, M. 2020. Arctic mid-winter phytoplankton growth revealed by autonomous profilers. *Science Advances* **6**(39). DOI: <http://dx.doi.org/10.1126/sciadv.abc2678>.
- Randelhoff, A, Oziel, L, Massicotte, P, Bécu, G, Galí, M, Lacour, L, Dumont, D, Vladoiu, A, Marec, C, Bruyant, F, Houssais, MN, Tremblay, JE, Deslongchamps, G, Babin, M. 2019. The evolution of light and vertical mixing across a phytoplankton ice-edge

- bloom. *Elementa: Science of the Anthropocene* **7**: 20. DOI: <https://doi.org/10.1525/elementa.357>.
- Rösel, A, Kaleschke, L, Birnbaum, G.** 2012. Melt ponds on Arctic sea ice determined from MODIS satellite data using an artificial neural network. *The Cryosphere* **6**(2): 431. DOI: <http://dx.doi.org/10.5194/tc-6-431-2012>.
- Schaaf, CB, Gao, F, Strahler, AH, Lucht, W, Li, X, Tsang, T, Strugnell, NC, Zhang, X, Jin, Y, Muller, JP, Lewis, P, Barnsley, M, Hobson, P, Disney, M, Roberts, G, Dunderdale, M, Doll, C, d'Entremont, RP, Hu, B, Liang, S, Privette, JL, Roy, D.** 2002. First operational BRDF, albedo nadir reflectance products from MODIS. *Remote Sensing of Environment* **83**(1–2): 135–148. DOI: [http://dx.doi.org/10.1016/S0034-4257\(02\)00091-3](http://dx.doi.org/10.1016/S0034-4257(02)00091-3).
- Schaaf, CLB, Liu, J, Gao, F, Strahler, AH.** 2011. MODIS Albedo and Reflectance Anisotropy products from Aqua and Terra. *Land Remote Sensing and Global Environmental Change: NASA's Earth Observing System and the Science of ASTER and MODIS* **11**(Remote Sensing and Digital Image Processing Series): 3–37.
- Schaepman-Strub, G, Schaepman, ME, Painter, TH, Dangel, S, Martonchik, JV.** 2006. Reflectance quantities in optical remote sensing—Definitions and case studies. *Remote Sensing of Environment* **103**(1): 27–42. DOI: <http://dx.doi.org/10.1016/j.rse.2006.03.002>.
- Smedley, ARD, Evatt, GW, Mallinson, A, Harvey, E.** 2020. Solar radiative transfer in Antarctic blue ice: Spectral considerations, subsurface enhancement, inclusions, and meteorites. *The Cryosphere* **14**(3): 789–809. DOI: <http://dx.doi.org/10.5194/tc-14-789-2020>.
- Stamnes, K, Hamre, B, Stamnes, JJ, Ryzhikov, G, Biryulina, M, Mahoney, R, Hauss, B, Sei, A.** 2011. Modeling of radiation transport in coupled atmosphere-snow-ice-ocean systems. *Journal of Quantitative Spectroscopy and Radiative Transfer* **112**(4): 714–726. DOI: <http://dx.doi.org/10.1016/j.jqsrt.2010.06.006>.
- Stamnes, K, Hamre, B, Stamnes, S, Chen, N, Fan, Y, Li, W, Lin, Z, Stamnes J.** 2018. Progress in forward-inverse modeling based on radiative transfer tools for coupled atmosphere-snow/ice-ocean systems: A review and description of the AccuRT model. *Applied Sciences* **8**(12): 2682. DOI: <http://dx.doi.org/10.3390/app8122682>.
- Stamnes, K, Tsay, SC, Wiscombe, W, Jayaweera, K.** 1988. Numerically stable algorithm for discrete-ordinate-method radiative transfer in multiple scattering and emitting layered media. *Applied Optics* **27**(12): 2502–2509. DOI: <http://dx.doi.org/10.1364/AO.27.002502>.
- Stroeve, J, Vancoppenolle, M, Veysiere, G, Lebrun, M, Castellani, G, Babin, M, Karcher, M, Landy, J, Liston, GE, Wilkinson, J.** 2021. A multi-sensor and modeling approach for mapping light under sea ice during the ice-growth season. *Frontiers in Marine Science* **7**: 1253. DOI: <https://doi.org/10.3389/fmars.2020.592337>.
- Taskjelle, T, Hudson, SR, Granskog, MA, Hamre, B.** 2017. Modelling radiative transfer through ponded first-year Arctic sea ice with a plane parallel model. *The Cryosphere* **10**. DOI: <http://dx.doi.org/10.5194/tc-11-2137-2017>.
- Tschudi, MA, Maslanik, JA, Perovich, DK.** 2008. Derivation of melt pond coverage on Arctic sea ice using MODIS observations. *Remote Sensing of Environment* **112**(5): 2605–2614. DOI: <http://dx.doi.org/10.1016/j.rse.2007.12.009>.
- Verin, G, Dominé, F, Babin, M, Picard, G, Arnaud, L.** 2019. Metamorphism of Arctic marine snow during the melt season. Impact on albedo. *The Cryosphere Discussions*: 1–29. DOI: <http://dx.doi.org/10.5194/tc-2019-113>.
- Vermote, E, Roger, JC, Ray, JP.** 2015. MODIS User Guide Version 1.4. *NASA EOSDIS Processes DAAC MODIS Land surface reflectance science computing facility (Collection 6)*: 35. DOI: [http://dx.doi.org/10.5067/MODIS/MOD09A1.006\(Terra\),10.5067/MODIS/MYD09A1.006\(Aqua\)](http://dx.doi.org/10.5067/MODIS/MOD09A1.006(Terra),10.5067/MODIS/MYD09A1.006(Aqua)).
- Warren, SG.** 2019. Optical properties of ice and snow. *Philosophical Transactions of the Royal Society—Mathematical, Physical and Engineering Sciences* **377**(2146): 20180161. DOI: <http://dx.doi.org/10.1098/rsta.2018.0161>.
- Warren, SG, Brandt, RE.** 2008. Optical constants of ice from the ultraviolet to the microwave: A revised compilation. *Journal of Geophysical Research* **113**(D14). DOI: <http://dx.doi.org/10.1029/2007jd009744>.
- Warren, SG, Brandt, RE, O'Rawe Hinton, P.** 1998. Effect of surface roughness on bidirectional reflectance of Antarctic snow. *Journal of Geophysical Research: Planets* **103**(E11): 25789–25807. DOI: <http://dx.doi.org/10.1029/98je01898>.
- Wright, NC, Polashenski, CM.** 2020. How machine learning and high-resolution imagery can improve melt pond retrieval from MODIS over current spectral unmixing techniques. *Journal of Geophysical Research: Oceans* **125**(2). DOI: <http://dx.doi.org/10.1029/2019jc015569>.
- Yackel, JJ, Nandan, V, Mahmud, M, Scharien, R, Kang, JW, Geldsetzer, T.** 2018. A spectral mixture analysis approach to quantify Arctic first-year sea ice melt pond fraction using QuickBird and MODIS reflectance data. *Remote Sensing of Environment* **204**: 704–716. DOI: <http://dx.doi.org/10.1016/j.rse.2017.09.030>.

**How to cite this article:** Laliberté, J, Rehm, E, Hamre, B, Goyens, C, Perovich, DK, Babin, M. 2022. A method to derive satellite PAR albedo time series over first-year sea ice in the Arctic Ocean. *Elementa: Science of the Anthropocene* 10(1). DOI: <https://doi.org/10.1525/elementa.2020.00080>

**Domain Editor-in-Chief:** Jody W. Deming, University of Washington, Seattle, WA, USA

**Associate Editor:** Kevin R. Arrigo, Department of Earth System Science, Stanford University, Stanford, CA, USA

**Knowledge Domain:** Ocean Science

**Part of an Elementa Special Feature:** Green Edge

**Published:** May 25, 2022    **Accepted:** April 9, 2022    **Submitted:** June 29, 2020

**Copyright:** © 2022 The Author(s). This is an open-access article distributed under the terms of the Creative Commons Attribution 4.0 International License (CC-BY 4.0), which permits unrestricted use, distribution, and reproduction in any medium, provided the original author and source are credited. See <http://creativecommons.org/licenses/by/4.0/>.



*Elem Sci Anth* is a peer-reviewed open access journal published by University of California Press.

OPEN ACCESS 